Design and Fabrication of Sharp Bend Photonic Crystal Slab Waveguides

by

Solomon Assefa

Submitted to the
Department of Electrical Engineering and Computer Science and
Department of Physics

in Partial Fulfillment of the Requirements of the
Degree of Bachelor of Science in Electrical Engineering and Computer Science,
Degree of Master of Engineering in Electrical Engineering and Computer Science
and
Degree of Bachelor of Science in Physics
at the Massachusetts Institute of Technology
May 11, 2001

Copyright 2001 Solomon Assefa. All rights reserved.

The author hereby grants to M.I.T. permission to reproduce and
distribute publicly paper and electronic copies of this thesis
and to grant others the right to do so.

BARKER

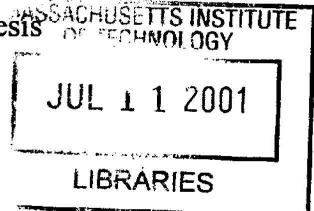

Author...

Solomon Assefa
Department of Electrical Engineering and Computer Science
Department of Physics
May 11, 2001

Certified by...

Leslie A. Kolodziejski
Professor of Electrical Engineering and Computer Science
Thesis Supervisor

Accepted by...

Arthur C. Smith
Chairman, E.E.C.S. Department Committee on Graduate Theses

Design and Fabrication of Sharp Bend Photonic Crystal Slab Waveguides

by

Solomon Assefa

Submitted to the
Department of Electrical Engineering and Computer Science
and
Department of Physics

May 11, 2001

In Partial Fulfillment of the Requirements of the
Degree of Bachelor of Science in Electrical Engineering and Computer Science,
Degree of Master of Engineering in Electrical Engineering and Computer Science
and
Degree of Bachelor of Science in Physics

Abstract

A periodic arrangement of atoms in a crystal presents a periodic potential for electrons. The bragg diffraction of electrons from the atoms may lead to a band gap, which represents a range of frequencies the electrons cannot have in the crystal. An analogous effect takes place in photonic crystals, which are periodic arrangement of layers of dielectric media. Scattering at the interface of the different layers produces a band gap for photons.

The current effort to make integrated optical chips requires guiding light around sharp corners with a radius of curvature on the order of a wavelength. Photonic crystals serve this purpose by providing efficient sharp bend waveguides. An array of defects in a photonic crystal localizes modes in the band gap. This effect is used to build linear and 90° bend waveguides.

Thesis Supervisor: Leslie Kolodziejski
Title: Professor of Electrical Engineering and Computer Science

Acknowledgement

I would like to thank my advisor Professor Leslie Kolodziejski for the help and guidance she has given me. I have been working with Leslie since I joined her group as a U.R.O.P. student in my junior year. The collaborative effort and the good spirit she promotes within her group and with other groups has contributed towards my education.

I would like to thank Dr. Gale Petrich for sharing with me his expertise in all aspects of my research. He is an invaluable resource of information in the theory and fabrication of III-V material systems.

I would like to thank Alexei Erchak for familiarizing me with all the labs at M.I.T. and for helping me understand the different fabrication processes. I have learned a lot from the discussions that we have everyday. I would also like to thank group members Aleksandra Markina and Reginald Briant. Additional thanks are extended to Mark Mondol, Jim Daley, and Prof. H. Smith.

Finally, my deepest gratitude goes to my parents, brothers, sisters and my friends who have encouraged me throughout my MIT experience. You have made my life very enjoyable.

Table of Contents

Chapter I

I. Introdution....................9

II. Maxwell's Equations in Dielectric Media....................11

III. Methods of Computation....................13

IV. Lattice Structure of Photonic Crystals....................16

V. Bloch States in Photonic Crystals....................20

VI. Symmetry of Modes in Photonic Crystals....................23

VII. Photonic Band Gaps....................24

VIII. Defects in Photonic Crystals....................26

IX. Photonic Crystal Slab Waveguides....................28

Chapter II

Device Design....................32

Chapter III

Fabrication

I. Epitaxial Growth and E-Beam Evaporation....................38

II. Direct Write Electron Beam Lithography....................41

III. Photolithography....................45

IV. Etching....................50

V. Oxidation....................60

Chapter IV

Conclusion and Future Work

I. Fabrication conclusion

a. Electron Beam Lithography and Photolithography....................61

b. Deep Etch..64

c. Process Flow...65

II. Future Work

a. Lapping and Cleaving...66

b. Testing PBG Devices..66

Reference...70

List of Figures

Figure 1. Dielectric layers with discrete translational symmetry. This periodic system has a lattice constant a and a repeated unit cell (the wire box) in the x-direction........................17

Figure 2. a) real space square lattice structure b) reciprocal square lattice structure 19

Figure 3. Construction of the brillouin zone (shaded region) 23

Figure 4. Two dimensional photonic crystal made of rods with lattice constant **a** and diameter **d**........24

Figure 5. Band diagram for the periodic structure given in Figure 1. $\varepsilon_1 = \varepsilon_2$ in (a); $\varepsilon_1 = 12$ and $\varepsilon_2 = 13$ in (b); $\varepsilon_1 = 1$ and $\varepsilon_2 = 13$ in (c)...25

Figure 6. a) defect is created in a 1D PBG by reducing the thickness of the middle stack b) defect is created in a 2D PBG by reducing the diameter of he middle dielectric cylinder...................27

Figure 7. A straight waveguide made of a linear defect of rods whose radii is smaller than the radii of the surrounding array of PBG cylinders 30

Figure 8. A sharp 90° bend photonic crystal slab waveguide created using rods of smaller radii..........31

Figure 9. Slab with a) uniform low-index dielectric background b) periodic low-index dielectric background...32

Figure 10. Asymmetric slab with low index stilts and caps...34

Figure 11. Band diagram for the asymmetric structure design (shaded region indicates the light cone)...36

Figure 12. PBG test structures with varying number of columns a) 9x3 b) 9x5 c) 9x7 d) 9x9............37

Figure 13. Initial material system of PBG structure...39

Figure 14. SEM of material system showing the grown structure of AlGaAs, GaAs, and the evaporated SiO_2 which is etched to make a cross shaped alignment mark..41

Figure 15. a) PMMA before exposure b) PMMA after exposure c,d) SEM of patterned PMMA with average hole size of 300 nm and input waveguide width of 1 μm..44

Figure 16. Sample a) after nickel evaporation b) after nickel liftoff..45

Figure 17. SEM of a sample after UV exposure. Figure shows some of the mask patterns that have been transferred to the photoresist..47

Figure 18. Sample a) after spinning photoresist b) after exposure and development..........................49

Figure 19. Sample after a) nickel evaporation b, c) nickel liftoff..49

Figure 20. a) sample after oxide etch b) crossection of (a) c) sample after nickel wet etch d) cross section of (c) 52

Figure 21. SEM of oxide mask after nickel wet etch (the nickel has not been completely lifted off the sidewall)....................52

Figure 22. a) sample after GaAs/AlGaAs etch b) cross section of (a)....................53

Figure 23. GaAs/AlGaAs etch data in NSL....................55

Figure 24. GaAs/AlGaAs etch in EML....................58

Figure 25. Final profile of PBG structure....................60

Figure 26. Misaligned cross shaped alignment marks (left); the background cross is written by E-beam and covered with nickel while the cross on the foreground is unexposed photoresist. Alignment of 1 μm lines (right). The left section is exposed photoresist lines while the right section is E-beam written and nickel coated lines....................61

Figure 27. Stitching error between two field written with two different beam currents (left) and stitching error between two fields written with the same beam current (right)....................63

Figure 28 a) 15 minutes straight etch of GaAs/AlGaAs layers (no interval)....................64

Figure 28 b) Interval Etch of GaAs/AlGaAs layers....................65

Figure 29. Linear PBG waveguide....................67

Figure 30. a) a total 180° PBG bend with straight input and output couplers b) a 90° PBG bend with a curved output coupler....................68

Figure 31. Tapered input and output coupling waveguides....................69

List of Tables

Table I. NSL Etch Results..56

Table II. EML Etch Results..59

Chapter I

I. Introduction

A periodic arrangement of dielectric materials with different indices of refraction, called a photonic crystal, creates a photonic band gap (PBG), that represents a frequency range where light is forbidden from propagating. Photonic crystals have led to new ways of controlling light. To this end, many groups are trying to fabricate three dimensional photonic crystals that have a complete band gap in all directions of propagation. For example, three dimensionally periodic structures can be made easily by using block copolymers[1], but these structures exhibit very small index contrast which results in a narrow band gap. The necessary index contrast can be achieved by planar growth or deposition of a layered structure. However, the planar nature of the growth makes the fabrication steps difficult because of the complex connectivity and alignment requirements.[2]

Alternatively, photonic crystal slabs can be used to approximate the properties of three dimensional photonic crystals. Photonic crystal slabs are two-dimensionally (2D) periodic structures that have a band gap for propagation in a plane and also use index guiding to confine light in the third dimension. Photonic crystal slabs are different from 2D photonic crystals due to the presence of a light cone, which is the projection of radiation modes arising from the index confinement in the vertical direction.

A periodic arrangement of dielectric rods with finite height in air results in a photonic crystal slab. The band gap of the structures is defined as a range of frequencies in

which no guided modes exist. However, there is still some radiation at those frequencies due to the light cone, which results from the higher effective index in the slab than in the background regions.

Photonic crystals have many applications in modern optoelectronics technology. Small scale optical signal processing requires waveguiding of an optical signal around sharp bends with a radius of curvature on the order of an optical wavelength. Conventional waveguiding is the result of total internal reflection at the interface between the high refractive index guiding layer and its low-index surroundings. However, waveguiding bends in the conventional index contrast waveguides may cause large optical losses depending on the radius of curvature of the bend.

Efficient waveguides with small radius of curvature are being created by introducing a row of smaller diameter dielectric cylinders, called a line defect, into a photonic crystal composed of an array of cylindrical rods. The 2D array of dielectric rods, which surrounds the line defect, creates a PBG. Thus, an optical signal with a frequency in the PBG has its energy confined inside the line defect. The radius of the cylinders in the line defect remains large enough to provide index guiding in the direction normal to the plane of periodicity of the crystal. Localization of the defect mode inside the line defect allows guiding around sharp corners including a 90^0 bend with low loss. This thesis concentrates on the design and fabrication of waveguides using photonic crystals.

II. Maxwell's Equations in Dielectric Media

The propagation of waves in dielectric media is governed by Maxwell's equations. These equations can be expressed as follows:

$$\nabla \bullet \bar{D}(\bar{r}, t) = \rho \quad \text{(EQ 1)}$$

$$\nabla \bullet \bar{B}(\bar{r}, t) = 0 \quad \text{(EQ 2)}$$

$$\nabla \times \bar{E}(\bar{r}, t) = -\frac{\partial}{\partial t}\bar{B}(\bar{r}, t) \quad \text{(EQ 3)}$$

$$\nabla \times \bar{H}(\bar{r}, t) = \frac{\partial}{\partial t}\bar{D}(\bar{r}, t) + \bar{J}(\bar{r}, t) \quad \text{(EQ 4)}$$

where $\bar{E}(\bar{r}, t)$ is the electric field strength, $\bar{H}(\bar{r}, t)$ is the magnetic field strength, $\bar{D}(\bar{r}, t)$ is the electric displacement, and $\bar{B}(\bar{r}, t)$ is the magnetic flux density.

Photonic crystal slabs are created using material that can be modeled as isotropic and low loss, which implies $\bar{D}(\bar{r}, t) = \varepsilon(r)[\bar{E}(\bar{r}, t)]$, where $\varepsilon(r)$ is approximated as real and constant.[3] We consider source free regions and let the permeability to be unity so that $\bar{B}(\bar{r}, t) = \bar{H}(\bar{r}, t)$. Using these observations, Maxwell's equations can be rewritten as:

$$\nabla \bullet \varepsilon(r)\bar{E}(\bar{r}, t) = 0 \quad \text{(EQ 5)}$$

$$\nabla \bullet \bar{H}(\bar{r}, t) = 0 \quad \text{(EQ 6)}$$

$$\nabla\times\bar{E}(\bar{r},t) = -\frac{\partial}{\partial t}\bar{H}(\bar{r},t) \quad \text{(EQ 7)}$$

$$\nabla\times\bar{H}(\bar{r},t) = \varepsilon(r)\frac{\partial}{\partial t}\bar{E}(\bar{r},t) \quad \text{(EQ 8)}$$

These equations are best solved by time-harmonic fields. These monochromatic waves or continuous waves (CW) are useful because (i) they can be easily used to eliminate the time dependence in the equations, (ii) they cover the whole spectrum of the electromagnetic waves, (iii) Fourier analysis can be used to understand the time-domain phenomena, and (iv) any solution can be built by combining the time-harmonic solutions through Fourier analysis.[4]

The time harmonic fields with angular frequency ω can be represented as

$$\bar{E}(\bar{r},t) = Re\{\bar{E}(\bar{r})\}e^{-iwt} \quad \text{(EQ 9)}$$

$$\bar{H}(\bar{r},t) = Re\{\bar{H}(\bar{r})\}e^{-iwt} \quad \text{(EQ 10)}$$

Substituting these fields into EQ 7 and EQ 8 gives time independent equations

$$\nabla\times\bar{H}(r,t) = -i\omega\varepsilon(r)\bar{E}(\bar{r}) \quad \text{(EQ 11)}$$

$$\nabla\times\bar{E}(r,t) = i\omega\bar{H}(\bar{r}) \quad \text{(EQ 12)}$$

By decoupling the two equations, the final expression in terms of $\bar{H}(\bar{r})$ becomes

$$\nabla\times\left(\frac{1}{\varepsilon(r)}\nabla\times\bar{H}(\bar{r})\right) = \omega^2\bar{H}(\bar{r})\,. \quad \text{(EQ 13)}$$

III. Methods of Computation

Light propagation and confinement in photonic crystals can be analyzed using a frequency-domain approach or a time-domain approach. In the frequency-domain approach, Maxwell's equations are decoupled using time-harmonic modes. This approach is important in determining the band structure of photonic crystals by writing the fields as a linear combination of eigenmodes.

The detailed treatment of this approach, summarized below, is given in a paper by Whittaker.[5] The approach uses the fact that $\varepsilon(r)$ is periodic, which lets us expand the transverse magnetic field into transverse plane waves summed over reciprocal lattice vectors G:

$$H(r, z) = \sum_{G} \tilde{H}_k(G, z) e^{i(k+G) \bullet r} \tag{EQ 14}$$

We also define a Fourier space vector $h(z) = [\tilde{H}_k(G_1, z), \tilde{H}_k(G_2, z), \ldots]^T$. From the Fourier expansion of the dielectric function, we define $\hat{\varepsilon}_{GG'} = \tilde{\varepsilon}(G - G')$, which is the dielectric matrix. Moreover, we define the inverse of the dielectric function as $\eta(r) = \varepsilon^{-1}(r)$, which has a Fourier expansion $\tilde{\eta}(G)$ and matrix representation $\hat{\eta}$.

The z-direction propagating wave can be expanded in terms of symmetric pair of basis states, ϕ_x and ϕ_y, as follows:

$$H(r,z) = \sum_G \Big(\phi_x(G)\Big[\hat{x} - \frac{1}{q}(k_x + G_x)\hat{z}\Big] + \phi_y(G)\Big[\hat{y} - \frac{1}{q}(k_y + G_y)\hat{z}\Big]\Big) e^{i(k+G)\bullet r + iqz} \quad \text{(EQ 15)}$$

By defining vectors $\phi_x = [\phi_x(G_1), \phi_x(G_2), \ldots]^T$ and $\phi_y = [\phi_y(G_1), \phi_y(G_2), \ldots]^T$, we can translate the above equation into a momentum representation as

$$h(z) = e^{iqz}\Big\{\phi_x\hat{x} + \phi_y\hat{y} - \frac{1}{q}(k_x\phi_x + k_y\phi_y)\Big\} \quad \text{(EQ 16)}$$

where $\hat{k}_x, \hat{k}_y$ are diagonal matrices with $(\hat{k}_x)_{GG} = (k_x + G_x)$ and $(\hat{k}_y)_{GG} = (k_y + G_y)$. The elements of the matrices are $k_x + G_x$ and $k_y + G_y$, which are propagation vectors in the plane of periodicity. By substituting the expression for the magnetic field into EQ 12, the expression for the electric field becomes

$$e(z) = \frac{1}{q}e^{iqz}\hat{\eta}\{[\hat{k}_y\hat{k}_x\phi_x + (q^2 + \hat{k}_y\hat{k}_x)\phi_y]\hat{x} - [\hat{k}_x\hat{k}_y\phi_y + (q^2 + \hat{k}_x\hat{k}_x)\phi_x]\hat{y} + q[\hat{k}_y\phi_x - \hat{k}_x\phi_y]\hat{z}\} \quad \text{(EQ 17)}$$

Substituting EQ 18 and EQ 19 into EQ 11 yields

$$\omega^2\phi_x = [\hat{k}_y\hat{\eta}\hat{k}_y + \hat{\eta}(q^2 + \hat{k}_x\hat{k}_x)]\phi_x + [\hat{\eta}\hat{k}_x\hat{k}_y - \hat{k}_y\hat{\eta}\hat{k}_x]\phi_y \quad \text{(EQ 18)}$$

$$\omega^2\phi_y = [\hat{k}_x\hat{\eta}\hat{k}_x + \hat{\eta}(q^2 + \hat{k}_y\hat{k}_y)]\phi_y + [\hat{\eta}\hat{k}_y\hat{k}_x - \hat{k}_x\hat{\eta}\hat{k}_y]\phi_x \quad \text{(EQ 19)}$$

In block matrix form, this becomes[5]

$$\left\{\begin{bmatrix}\hat{\eta} & 0\\ 0 & \hat{\eta}\end{bmatrix}\left[q^2+\begin{bmatrix}\hat{k}_x\hat{k}_x & \hat{k}_x\hat{k}_y\\ \hat{k}_y\hat{k}_x & \hat{k}_y\hat{k}_y\end{bmatrix}\right]+\begin{bmatrix}\hat{k}_y\hat{\eta}\hat{k}_y & -\hat{k}_y\hat{\eta}\hat{k}_x\\ -\hat{k}_x\hat{\eta}\hat{k}_y & \hat{k}_x\hat{\eta}\hat{k}_x\end{bmatrix}\right\}\begin{bmatrix}\phi_x\\ \phi_y\end{bmatrix} = \omega^2\begin{bmatrix}\phi_x\\ \phi_y\end{bmatrix} \tag{EQ 20}$$

These eigenstates are used as basis states to construct the fields (EQ 18) in each layer of the structure. The field is expressed in a matrix as a combination of forward and backward propagating waves while the boundary conditions are set at the interfaces of the structure. Then, the matrix, call an S-matrix, is used to relate and determine the vectors and the amplitudes of forward and backward scattering waves in the different layers.[5] Fast and optimized numerical simulations are used to solve Maxwell's equations and get band structures of photonic crystals in the frequency domain.[6]

Time-domain approach is useful in determining the transient properties and the quality factor of localized modes. A time domain finite difference method can be employed to study the evolution of fields in photonic crystals.[7] For TM waves with the electric field pointing in the z direction, the wave equation is written as

$$\frac{\partial^2}{\partial x^2}E(x,y)+\frac{\partial^2}{\partial y^2}E(x,y) = \varepsilon(x,y)\frac{\partial^2}{\partial t^2}E(x,y) \tag{EQ 21}$$

This can be changed into difference equations by discretization of space into units of Δs and time into units of Δt.[8] Taking n to be time index, i, j to be space indices, the field $E(i\Delta s, j\Delta s, n\Delta t)$ is written as $E^n{}_{i,j}$, and the discrete dielectric constant $\varepsilon(i\Delta s, j\Delta s, n\Delta t)$ is written as ε_{ij}. Using this and by approximating the derivative at each lattice point as a centered difference, EQ 14 can be approximated into a difference equation as

$$\frac{E^n_{i+1,j} - 2E^n_{i,j} + E^n_{i-1,j}}{(\Delta s)^2} + \frac{E^n_{i,j+1} - 2E^n_{i,j} + E^n_{i,j-1}}{(\Delta s)^2} = (\varepsilon_{i,j})\frac{E^{n+1}_{i,j} - 2E^n_{i,j} + E^{n-1}_{i,j}}{(\Delta t)^2} \tag{EQ 22}$$

This equation is solved for $E^{n+1}_{i,j}$ and used to update the previous time values. Since computation is done in finite-sized unit cells, information outside the cell is not available and the fields at the edges must be updated using boundary conditions, such as Mur's second order absorbing boundary condition in order to minimize back reflection into the cell.[9] A detailed treatment of boundary conditions and the potential problems of the FDTD approach is given by Winn *et al.*[10]

IV. Lattice Structure of Photonic Crystals

Photonic crystals have discrete translational symmetry. For example, a distributed Bragg reflector (DBR) which is constructed from alternating layers of two dielectric materials with different refractive indices and a layer thickness of $\frac{\lambda}{4}$ as shown in Figure 1 is a simple 1 dimensional (1D) photonic crystal. In two dimensional (2D) photonic crystals, the periodicity is along two axes and can consist of an array of high index columns surrounded by a low index material or an array of air holes in a high dielectric material.

The **lattice** in photonic crystals can be characterized by using the lattice vector $\bar{R}$,

$$\bar{R} = n_1\bar{a}_1 + n_2\bar{a}_2 + n_3\bar{a}_3 \qquad \text{(EQ 23)}$$

where $\bar{a}_i$ are the **primitive lattice vectors**.

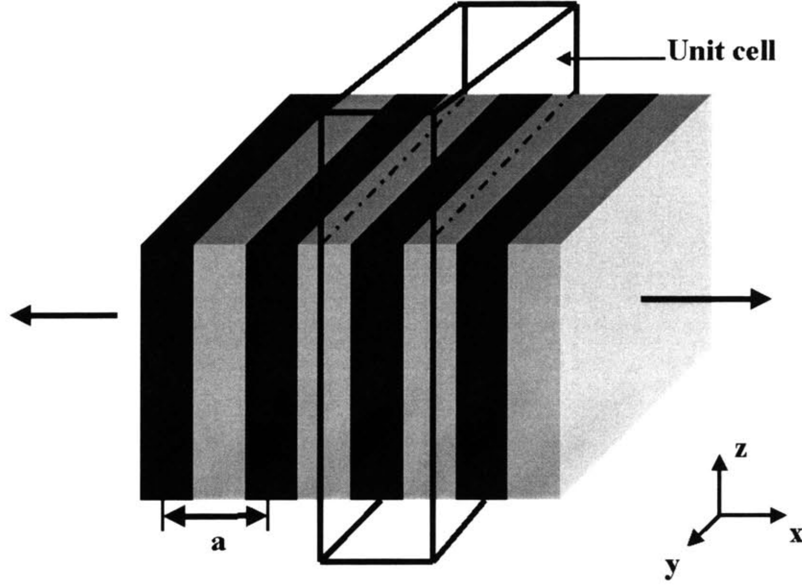

Figure 1. Dielectric layers with discrete translational symmetry. This periodic system has a lattice constant a and a repeated unit cell (the wire box) in the x-direction

The lattice vectors are defined as

$$\bar{a}_i = a\hat{r}_i \ . \qquad \text{(EQ 24)}$$

The **basis** is the underlying pattern that is repeated with lattice constant *a*. The primitive cell is the smallest unit cell containing the basis that can be repeated. The one dimensional photonic crystal given in Figure 1 has a dielectric constant $\varepsilon(\bar{r})$ such that

$$\varepsilon(\bar{r}) = \varepsilon(\bar{r} + \bar{R}_i), \qquad \text{(EQ 25)}$$

where $\bar{R} = n\overline{a_i}$.

Taking the Fourier transform of both sides of EQ 25 gives

$$\varepsilon(\bar{r}) = \int_{-\infty}^{\infty} \varepsilon(\bar{q}) e^{i\bar{q} \bullet \bar{r}} \frac{dq^3}{(2\pi)^3} \quad \text{(EQ 26)}$$

$$\begin{aligned} \varepsilon(\bar{r} + \bar{R}_i) &= \int_{-\infty}^{\infty} \varepsilon(\bar{q}) e^{i\bar{q} \bullet (\bar{r} + \bar{R}_i)} \frac{dq^3}{(2\pi)^3} \\ &= e^{i\bar{q} \bullet (\bar{R})} \int_{-\infty}^{\infty} \varepsilon(\bar{q}) e^{i\bar{q} \bullet \bar{r}} \frac{dq^3}{(2\pi)^3} \end{aligned} \quad \text{(EQ 27)}$$

From this, it follows that EQ 25 is true only if

$$e^{i\bar{K} \bullet \bar{R}} = 1 , \quad \text{(EQ 28)}$$

which is equivalent to saying,

$$\bar{K}_j \bullet \bar{R}_i = 2\pi(l) \quad \text{(EQ 29)}$$

where l is an integer.[11]

$\bar{K}_j$ is called the reciprocal lattice vector, and is written in terms of primitive reciprocal lattice vectors as

$$\bar{K}_j = m_1 \bar{b}_1 + m_2 \bar{b}_2 + m_3 \bar{b}_3 \quad \text{(EQ 30)}$$

with the condition that

$$\bar{a}_i \bullet \bar{b}_j = 2\pi\delta_{ij} \quad \text{(EQ 31)}$$

By construction, $\bar{b}_1 = 2\pi \frac{\bar{a}_2 \times \bar{a}_3}{\bar{a}_1 \bullet (\bar{a}_2 \times \bar{a}_3)}$, $\bar{b}_2 = 2\pi \frac{\bar{a}_3 \times \bar{a}_1}{\bar{a}_1 \bullet (\bar{a}_2 \times \bar{a}_3)}$,

$\bar{b}_3 = 2\pi \frac{\bar{a}_1 \times \bar{a}_2}{\bar{a}_1 \bullet (\bar{a}_2 \times \bar{a}_3)}$.

For orthogonal primitive lattice vectors, as in a 2D photonic crystal with a rectangular lattice of rods, the reciprocal lattice vector becomes

$$\bar{K}_j = m_1 \frac{2\pi}{a_1} \hat{r}_1 + m_2 \frac{2\pi}{a_2} \hat{r}_2 + m_3 \frac{2\pi}{a_3} \hat{r}_3 \quad \text{(EQ 32)}$$

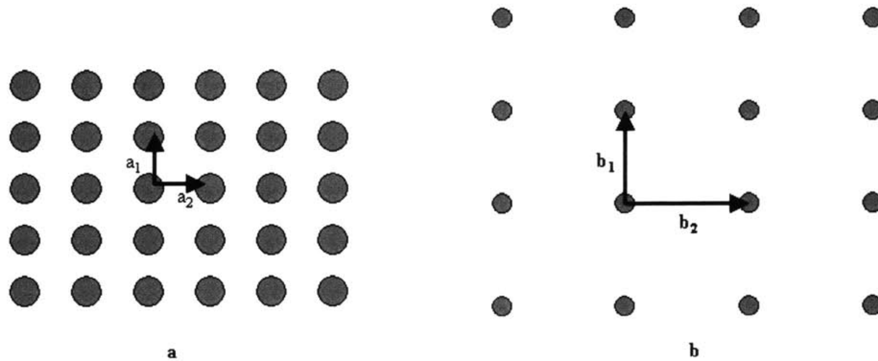

Figure 2. a) real space square lattice structure b) reciprocal squre lattice structure

The reciprocal lattice can be constructed pictorially as well (Figure 2). Given the lattice of the structure, the basis can be identified. If the basis vectors are labelled as $\bar{a}_i$, then the

above equation tells us that the reciprocal lattice $\bar{b}_j$ is perpendicular to the lattice basis vectors where $i \neq j$.

V. Bloch States in Photonic Crystals

By making analogy to quantum mechanics, electromagnetism can be stated as an eigenvalue problem in the frequency-domain approach. If the result of an operation on a function is just the function itself, multiplied by some constant, then the function is called an **eigenfunction** or **eigenvector** of that operator, and the multiplicative constant is called the **eigenvalue**.[3] For the photonic crystals, the eigenfunction is the harmonic field *H(r)* and eigenvalue would be ω^2 (EQ 13).

In quantum mechanics, a Hermitian operator Ω acting on two field vectors A and B has the following property

$$(A, \Omega B) = (\Omega A, B) \qquad \text{(EQ 33)}$$

where (A,B), the inner product of normalized vector fields A and B, is given as

$$(A, B) = \int A^* \bullet B \, dr \qquad \text{(EQ 34)}$$

A Hermitian operator implies that the eigenfunctions are orthogonal and they have real eigenvalues. From EQ 13, an electromagnetic operator which takes the curl of an eigenfunction, divides the result by the dielectric constant, and takes the curl again is defined as

$$\Pi = \nabla\times\left(\frac{1}{\varepsilon(r)}\nabla\ \ x\right). \qquad \text{(EQ 35)}$$

By making an analogy to the Hamiltonian operator in quantum mechanics, it can be shown that Π is Hermitian as follows[3]

$$\begin{aligned}(A, \Pi B) &= \int A^* \bullet \nabla\times\left(\frac{1}{\varepsilon}\nabla\times B\right) dr \qquad \text{(EQ 36)}\\ &= \int(\nabla\times A)^* \bullet \frac{1}{\varepsilon}(\nabla\times B)\ dr\\ &= \int\left(\nabla\times\left(\frac{1}{\varepsilon}\nabla\times A\right)\right)^* \bullet B\\ &= (\Pi A, B)\end{aligned}$$

Thus, since H is an eigenfunction of Π, which is linear and Hermitian, H can be expressed as a linear combination of eigenmodes. For example, for two dimensional photonic crystals with k_x, k_y as the wavevectors in the direction of periodicity,

$$\begin{aligned}H_{k_x, k_y}(r) &= \sum_{m, n} c_{k_{x, m}}(z) c_{k_{y, n}}(z) e^{i(k_x + mb_x)x} e^{i(k_y + nb_y)y} \qquad \text{(EQ 37)}\\ &= e^{ik_y y} e^{ik_x x} \sum_{m, n} c_{k_{x, m}}(z) c_{k_{y, n}}(z) e^{imb_x x} e^{inb_y y}\\ &= e^{ik_y y} e^{ik_x x} u_{k_x}(x, z) u_{k_y}(y, z)\end{aligned}$$

where $u_{k_x}(x, z) = \sum_m c_{k_{x, m}}(z) e^{imb_x x}$ and $u_{k_y}(y, z) = \sum_n c_{k_{y, n}}(z) e^{inb_y y}$.

$c_{k_{x,m}}(z)$ and $c_{k_{y,n}}(z)$ are calculated by using the frequency domain approach, which results in an expression like EQ 18. Using the concept of reciprocal lattice, it can be deduced that $u(x+la, z) = u(x, z)$ and $u(y+la, z) = u(y, z)$.

The above is an example of Bloch's theorem and $u(x, z)$ is called a **Bloch state.** The equation implies that the Bloch frequencies $\omega(k_x)$ and $\omega\left(k_x + \frac{2\pi}{a}\right)$ are the same. It follows from Bloch's theorem that $E_n(k) = \frac{\hbar^2}{2m}\left(k + \frac{2\pi n}{a}\right)^2$. As a result, the extended zone band diagram representation can be replaced with a reduced zone, having the range $-\frac{\pi}{2} \le k \le \frac{\pi}{2}$, which is defined as the **first brillouin zone** (the edges are labelled by Γ, M ,X. Bloch frequencies imply that at a given *k* in the first brillouin zone there are bands of different energies $E_n(k)$ that are labeled by the band index *n*. Because *k* repeats itself outside the $[-\frac{\pi}{2},\frac{\pi}{2}]$ range, in the reduced zone representation the energy bands fold back into the Brillouin zone when they reach the zone edges. This is called band folding. The brillouin zone can be constructed pictorially from the reciprocal lattice. A basis is chosen as an origin and straight lines are drawn to the neighboring cells. Then, perpendic-

ular bisectors to these lines are drawn. As shown in Figure 3, the intersection of these perpendicular lines forms the first brillouin zone.

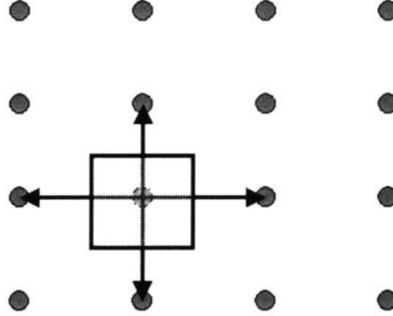

Figure 3. Construction of the brillouin zone (shaded rectangular region)

VI. Symmetry of Modes in Photonic Crystals

Electromagnetic modes in photonic crystals can be often characterized by their mirror symmetry. Any mode ψ can be characterized by its mirror symmetry. For a mirror reflection M, the mode is defined as **odd** if $M\psi = -\psi$ and **even** if $M\psi = \psi$.

For the two dimensional photonic crystal, the plane of periodicity is the x-y plane, and the axis of symmetry is the z-axis. The x-y mirror plane, called M_z, transforms $\hat{z}$ into $-\hat{z}$. If k is parallel to the plane M_z, reflection through the plane gives back the wavevector itself. This mirror is used to classify the modes as TE and TM.[3] For TE modes, $\bar{E} \cdot \bar{z} = 0$, and for TM modes, $\bar{H} \cdot \bar{z} = 0$.

VII. Photonic Band Gaps

A photonic band gap exists when there is a frequency gap between the minimum point of the upper energy band and maximum point of the lower energy band; no propagation modes exist in the gap regardless of the *k* values. The degeneracy at the symmetry points Γ, M, X is broken and the density of optical states in the gap is zero ($\rho(\omega) = 0$).

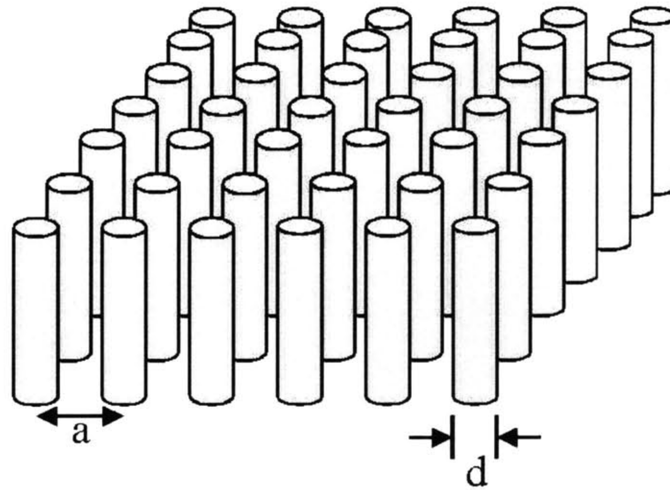

Figure 4. Two dimensional photonic crystal made of rods with lattice constant **a** and diameter **d**

For an infinite stack of dielectric layers with all of the layers having the same dielectric constant, the dispersion relationship gives two straight lines with slope $\frac{\Delta\omega}{\Delta k} = |1|$ in the extended zone representation. In the reduced zone, the folded bands meet either at the zone center or the zone edges. As a result, there is no band gap with a range of forbidden frequency for photons.

The effect of index contrast on band gaps can be seen from the electromagnetic variation theorem. The functional energy E_f is given as[3]

$$E_f = \frac{1}{2}\frac{(H, \Pi H)}{(H, H)} . \qquad \text{(EQ 38)}$$

By considering the effect of a small perturbation, we finally find that

$$E_f(H)) = \left(\frac{1}{2(H, H)}\right) \int \frac{1}{\varepsilon}\left|\frac{\omega}{c} D\right|^2 , \qquad \text{(EQ 39)}$$

where (H,H) is the inner product of the given fields. This is worked out in detail in reference 3. The equation gives the dependence of the energy bands on the index ($n = c\sqrt{\varepsilon}$ taking permeability μ to be unity). As ε increases $E_f(H)$ decreases, and as ε decreases $E_f(H)$ increases.

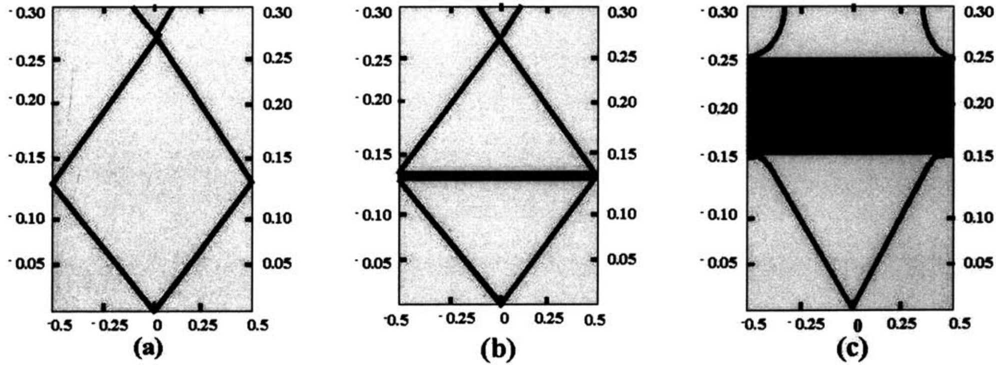

Figure 5. Band diagram for the periodic structure given in Figure 1. $\varepsilon_1 = \varepsilon_2$ in (a); $\varepsilon_1 = 12$ and $\varepsilon_2 = 13$ in (b); $\varepsilon_1 = 1$ and $\varepsilon_2 = 13$ in (c)

The gap is formed because the low energy modes are concentrated in the high index dielectric layer and the high energy modes are concentrated in the low index dielec-

tric layer. While a uniform dielectric layer does not have a band gap (Figure 5a), a dielectric composed of alternating layers with $\varepsilon = 12$ and $\varepsilon = 13$ results in the formation of a small gap (Figure 5b). Finally, when the contrast is increased from $\varepsilon = 1$ to $\varepsilon = 13$, a larger gap is formed between the bands as in Figure 5 c.

The existence of a gap means that photons with a frequency in the gap will not be able to propagate in the plane of periodicity. The modes that have gap frequency become evanescent, meaning that their wave vector becomes imaginary in the direction of periodicity. As a result, the transmitted Poynting vector ($\bar{S}_t$) becomes complex and the real part in the direction of propagation becomes zero, which implies the time-average power transmitted in that direction, $\langle \bar{S}_t \rangle$, is zero.

VIII. Defects in Photonic Crystals

A defect is created in a one dimensional photonic crystal when the thickness of one of the alternating stacks of dielectric layers is either increased or decreased, breaking the translational symmetry of the crystal as shown in Figure 6. The defect causes a mode, called a **defect mode**, to exist in the band gap.

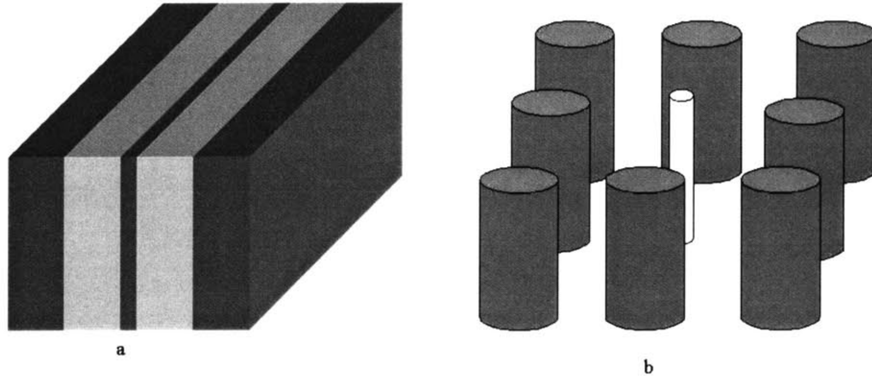

Figure 6. a) defect is created in a 1D PBG by reducing the thickness of the middle stack b) defect is created in a 2D PBG by reducing the diameter of he middle dielectric cylinder

For a 2D array of cylinders, a single defect is produced by increasing or decreasing the radius of one of the rods. The 2D array of periodic dielectric rods, which surrounds the defect, creates a PBG in which light within that range of frequencies cannot propagate. A mode with a frequency in the PBG becomes localized at the defect and decays exponentially away from the defect. It cannot couple to the nearby rods because the defect mode has a frequency inside the PBG. The defect mode energy increases as the refractive index of the defect decreases; modes get pushed up into the gap from the lower band. The energy decreases as the index of the defect increases; modes get pushed down from the upper band. These modes are calculated by using the supercell approximation method, in which a supercell consisting of a crystal with a defect is repeated periodically in space.[7]

IX. Photonic Crystal Slab Waveguides

In two dimensions, a waveguide can be created from a linear array of defects. Increasing or decreasing the radius of one of the rows or columns of the periodic square lattice or rods produces a linear defect. The 2D array of periodic rods, which surrounds the line defect, creates a PBG. The mode that couples to the defects has a frequency that is inside the PBG, which means the mode is forbidden from propagating anywhere else in the structure. As a result, the defect mode will not be able to couple to the surrounding rods. Instead, light will be forced to couple from one defect rod to the next defect rod which supports the same mode. Thus, the measured loss in this linear waveguide is primarily due to input and output coupling to the photonic crystal.

Photonic crystal slabs are 2D periodic structures that have a finite height. Guiding in the plane of propagation is due to the photonic crystal, while in the third dimension light is confined due to index contrast between the slab and the surrounding media. Hence, photonic crystal slabs are different from the ideal 2D photonic crystals discussed above, which are modeled with infinite height. The introduction of the light cone (a continuous region indicating all possible frequencies of the bulk background[12]) results from the index confinement in the z-direction; as a result, the presence of radiation modes prevents the band gap from being complete. Furthermore, the modes are classified as TE-like (even) and TM-like (odd) modes. The symmetry of the structure is broken due to the presence of the substrate (background region), which prevents the modes from being fully TE or TM. The thickness of the slab can be approximated as follows[12]:

$$h \sim \frac{1}{2\omega_{gap-bottom}\sqrt{\bar{\varepsilon}}}, \quad \text{(EQ 40)}$$

where $\omega_{gap-bottom}$ is the frequency of the band at the bottom of the gap in units of c/a, $\bar{\varepsilon}$ is the effective dielectric constant, and h is the height in units of a. EQ 40 simply implies that using a wavelength as a lengthscale of variation in field amplitude, the optimal thickness will be on the order of gap-bottom wavelength.[12] Photonic slab waveguides produce a practical way of creating three dimensional confinement, since the vertical index contrast can be achieved through planar growth and oxidation.

Photonic crystal slabs present a better alternative to conventional waveguiding, which is the result of total internal reflection at the interface between the high refractive index guiding layer and its low-index surrounding. These waveguides can be either single-mode or multi-mode. Waveguide bends in the conventional index-contrast waveguides may cause large optical losses depending on the radius of curvature of the bend relative to the wavelength of the guided light. The loss that is incurred at bends due to coupling to radiation modes is dependent on the radius of curvature and the index contrast of the material and the wavelength of the light being used.

In a photonic crystal slab, an efficient waveguide can be created by introducing a linear defect along one of the rows. The periodic structure creates a PBG for TM-like modes which prohibits the defect mode from escaping into the plane of the crystal. In the third dimension, the mode is index-confined and the size of the defects can be chosen to place the guided modes below the light line to prevent the coupling to radiation modes. As a result, the defect mode decays exponentially away from the defects and its energy is

heavily localized in the defects. Furthermore, the TM-like modes are localized around the rod in air, which implies guiding in a low-index material.

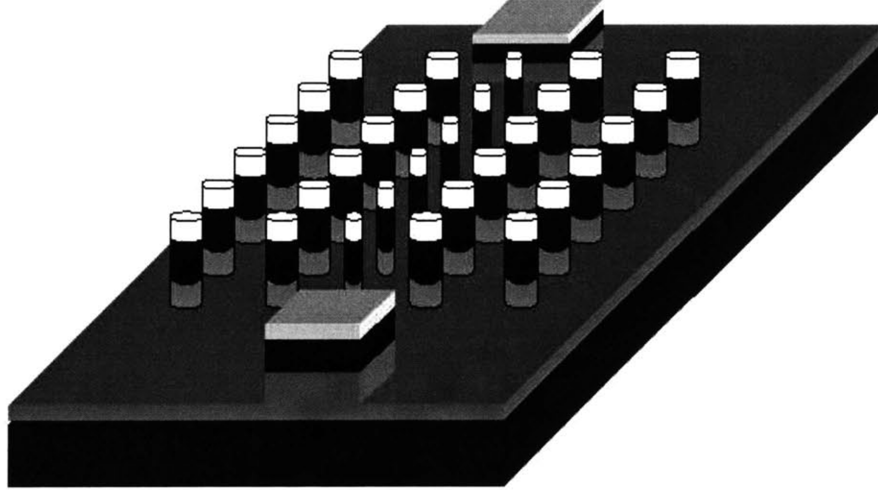

Figure 7. A straight waveguide made of a linear defect of rods whose radii is smaller than the radii of the surrounding array of PBG cylinders

Sharp 90° bends in the waveguides can be constructed in photonic crystal slabs as shown in Figure 8. There will be high transmission through the bend, because the defect mode does not couple to any of the other guided modes and is also confined vertically. As a result, photonic crystal slabs provide efficient waveguides. Again, loss comes from input and output coupling to the photonic crystal region. The transmission can be quantized by normalizing the measured transmission of the bend waveguide to the measured transmission of the linear waveguide.

A good model for sharp bends in photonic crystals is given by Mekis.[13] A sharp 90° bend can be modeled by two waveguide sections in the (10) and (01) direction, connected by another section in the (11) direction. The wavevectors can be labeled as $k_1(w)$

for the (10) and (01) directions and as $k_2(w)$ in the (11) direction. The transmission then can be modeled as a one dimensional scattering process. By using continuity of the electromagnetic field and an analogy of the Schrödinger equation, the derived reflection coefficient becomes

$$R(w) = \left[1 + \left(\frac{2k_1(w)k_2(w)}{[k_1^2(w) - k_2^2(w)]\sin[k_2(w)L]}\right)^2\right]^{-1}.$$

For a 90° bend, the effective length of the corner is extrapolated to be $L = 0.33\sqrt{2}a$; for guided modes with frequency below $\omega = 0.403 \times 2\pi\frac{c}{a}$, the simulated transmission is greater than 95%. For conventional dielectric guides that have index contrast of 3.5 to 1 with the surrounding, large radiation losses at the corner of a similar sharp 90° bend results in a power transmission of at most 30%.[13]

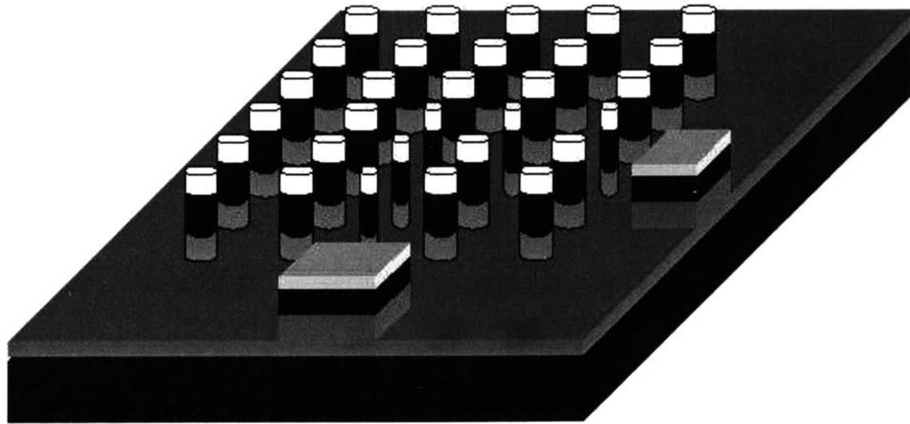

Figure 8. A sharp 90° bend photonic crystal slab waveguide created using rods of smaller radii

Chapter II

Device Design

In order to design the PBG waveguides, various structures were considered and simulated. The determining factors in choosing the final design were solid performance and amenability to fabrication. First, the design needs to have a band gap centered around a frequency of 0.323 (c/a) where a is 500 nm so that the device can operate at a wavelength of 1.55 μm; it also requires good localization of guided modes and a minimum mixing between the even and odd modes. Second, the design has to be feasible under the constraints of material systems and the limitation of current fabrication technology.

The first design considered was a slab of periodic rods sandwiched between uniform dielectric substrate as shown in Figure 9 a. The substrate which occupies the background regions above and below the array of rods has an index of refraction which is lower than the effective index of the slab.

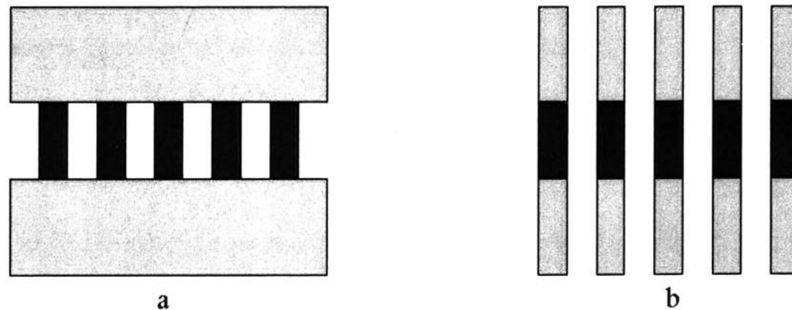

Figure 9. Slab with a) uniform low-index dielectric background
b) periodic low-index dielectric background

If the substrate is several wavelengths thick, it can be considered to have infinite thickness because the intensity of the guided modes dies off exponentially outside of the substrate. This index contrast between the slab and the substrate provides confinement in the vertical direction. Even though the modes can be classified as even or odd, they are somewhat less localized due to the smaller index contrast between the substrate and the slab.[2] The major disadvantage of this design is the difficulty of fabrication. If all the layers are grown first, then it will be difficult to make the rods by processing only the middle layer. Also, one might consider growing the lower substrate and the guiding layer, then doing the processing, and then growing or bonding the top substrate. Due to fabrication problems, the size scale of the rods and the size of the 2D array that is used here does not make the rods capable of supporting a thick substrate.

The second design considered was similar to the first, but with the background substrates patterned as shown in Figure 9b. The design leaves each rod with a dielectric layer above and below, which makes the structure more symmetric. The patterning of the background gives an effective index which is smaller than the substrate index in the first design, and leads to more confinement of the guided modes. Nevertheless, this is difficult to fabricate because of the nature of the material system being used despite the less complicated etching step. AlGasAs can be used as a low-index material below and above the guiding layer of GaAs. However, the top layer of AlGaAs which can be grown epitaxially will eventually oxidize when exposed to air during processing.

The final design is as shown in Figure 10. The structure has a guiding layer, which is sufficiently separated from the substrate by low index "stilts". Also, the rods have caps

on top of them, which roughly restores mirror symmetry back to the system. The mirror symmetry determines which modes (even or odd) form the PBG so that light can be polarized as TE or TM during testing. In order to classify the guided modes as even or odd, it is only necessary to preserve mirror symmetry where the guided modes have non-negligible amplitude.[2]

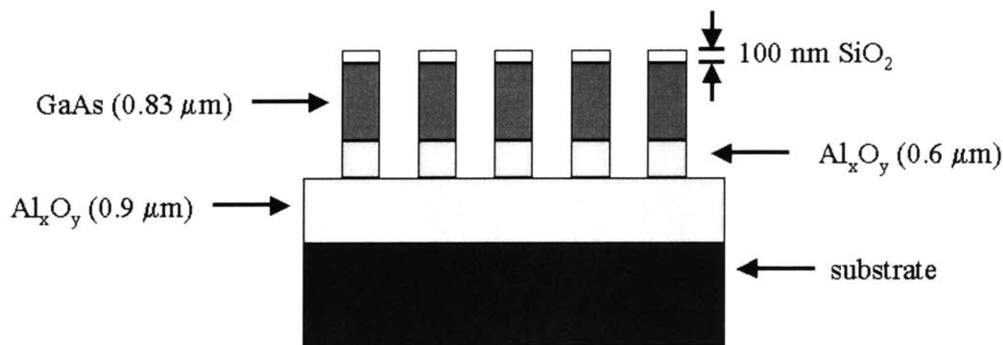

Figure 10. Asymmetric slab with low index stilts and caps

The thickness of the slab was also a factor in the design of the structure. If the slab is too thick, then higher-order modes will be created close to the lowest-order mode which will cause the gap to disappear. If the slab is thicker than a wavelength, higher order modes are created by forming horizontal nodal planes. On the other hand, making the slab very thin will cause the modes to be weakly guided and very close to the light cone. If the slab thickness less than half a wavelength (size of the lowest order mode), the confinement of the mode is very small. It is postulated that the optimal thickness is half the two-dimensional gap-bottom wavelength, because the wavelength is the lengthscale for variations in field amplitude at the given frequency (EQ 40).[2]

For this design, simulations were done using lattice constant (a) values that range from 450 nm to 650 nm; the simulated heights varied from $1.36a$ to $1.66a$ while the diameter d varied from $0.4a$ to $0.6a$. Both symmetric (GaAs rods with SiO_2 caps and stilts, or Al_xO_y caps and stilts) and asymmetric (GaAs rods with SiO_2 caps and Al_xO_y stilts) were simulated. From simulations of slab thickness and gap size, the optimal thickness for the structure was chosen to be 0.83 μm. Given that light with wavelength between 1390 nm and 1680 nm can be used in the testing setup and given that the thickness will be 0.83 μm, the best structures were determined to have a lattice constant of 500 nm with rod diameter of 300 nm. Using these values, another simulation was performed on the following structure: 100 nm thick SiO_2 cap, 0.83 μm thick GaAs guiding layer, 0.6 μm thick Al_xO_y stilts, 0.9 μm thick Al_xO_y layer, on a GaAs substrate. Figure 11 shows the calculated band structure. Even though the structure is asymmetric, the index of refraction of the cap and the stilts are very close (1.5 for SiO_2 and 1.6 for Al_xO_y). As a result, the extent of mirror symmetry increases and the guided modes can be classified as even and odd. The gap to midgap ratio for the odd modes for the above structure is found to be approximately 10%.

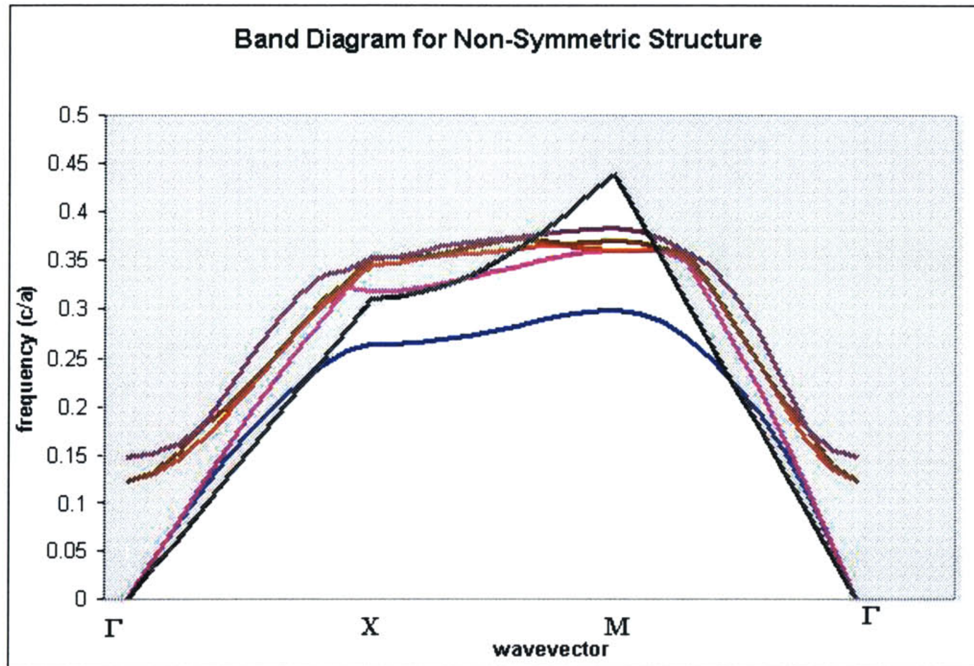

Figure 11. Band diagram for the asymmetric structure design (shaded region indicates the light cone)

Due to the small size, it is quite difficult to fabricate rods with an exact diameter of 300 nm. In order to be able to account for these errors and investigate the band edges, the rods were designed with diameter within the range of 0.7*d* and 1.3*d*, where d is 300 nm. Furthermore, the design varied the number of columns from one structure to another, so that it would be possible to see the increasing width of the photonic bandgap as the number of columns increases. As a method for normalization of data, straight dielectric waveguides were also included in the designed structures (Figure 12).

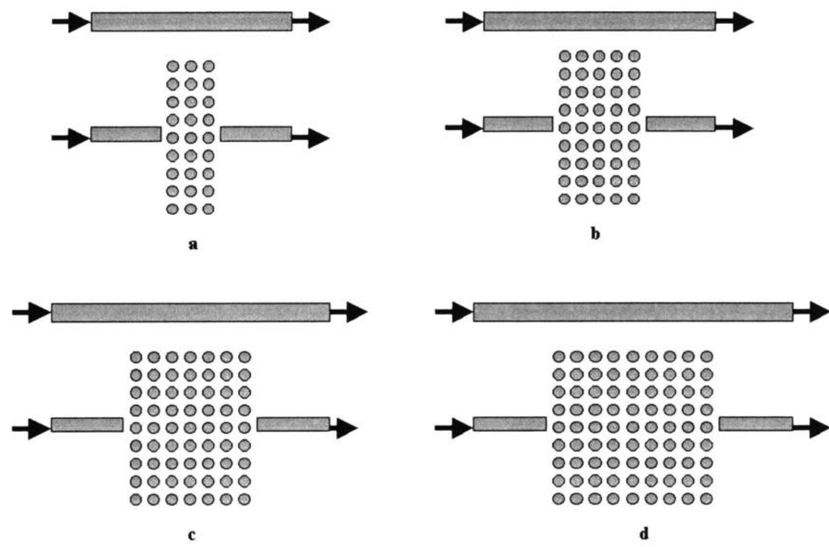

Figure 12. PBG test structures with varying number of columns a) 9x3 b) 9x5 c) 9x7 d) 9x9

Chapter III

I. Epitaxial Growth and E-Beam Evaporation

The first part of the process involves the use of Gas Source Molecular Bean Epitaxy (GSMBE). This growth technique, which can deposit layers with atomic resolution[14], is done in an ultra high vacuum (UHV) environment (10^{-10} torr base vacuum). The basic requirements of a GSMBE system are in situ sample heating and cleaning, and independently controlled sources for all constituent materials and dopants. High vacuum is achieved by baking and pumping the system at temperature ranging from 150 to 250°C, which will increase the vapor pressure of gases and water adsorbed on the inside walls of the chamber. Most Solid Source MBEs use ion pumps or adsorption cryopumps, while GSMBEs use turbomolecular pumps.

Sample growth is performed at the CBE laboratory using the Riber 32P system. First, the sample is loaded into the Intro chamber, which is the load lock for the system and has a base pressure of 10^{-8} torr. Then, the sample is moved into the Transfer chamber, which has a base pressure of 9×10^{-10} torr, and degassed at 210°C for one hour to remove the absorbed moisture on the sample and the sample holder. The sample is then moved into a Buffer chamber that lies between the Transfer chamber and growth reactor. The base pressure of the Buffer chamber is at 5×10^{-10} torr. Finally, the sample is moved into the Riber 32P growth chamber, which has a base pressure of 2×10^{-10} torr. The chamber contains elemental Ga, In, Al, Si and Be effusion cells and a AsH_3 and PH_3 cracker. Dur-

ing growth, the pressure increases to $2x10^{-5}$ due to the presence of cracked or thermally decomposed (at 900°C) AsH_3 and PH_3. For a GaAs substrate, the sample is heated at 600°C, Ga source at 1000°C, In source at 800°C, and Al source at 1120°C. Also, the Riber system is equipped with a Reflection High Energy Electron Diffraction (RHEED) which is used to characterize deposition rates and sample surface morphology, and an in situ spectroscopic ellipsometer.[15]

After the 300 μm thick p-type <100> GaAs substrate is baked and transferred into the growth chamber, a 1.5 μm thick $Al_{0.9}Ga_{0.1}As$ layer is epitaxially grown. GaAs and $Al_{0.9}Ga_{0.1}As$ are lattice matched, which means that they have the same lattice constant of 0.565 nm. As a result, stress/strain is not a problem in the growth. The composition can be varied by changing the AlGaAs cell temperature, which changes the flux ratio of the two types of atoms that arrive at the surface. By varying composition of Al and Ga, the index, electronic band gap, and some chemical properties can be varied. Next, a 0.85 μm thick GaAs layer is grown epitaxially on the $Al_{0.9}Ga_{0.1}As$.

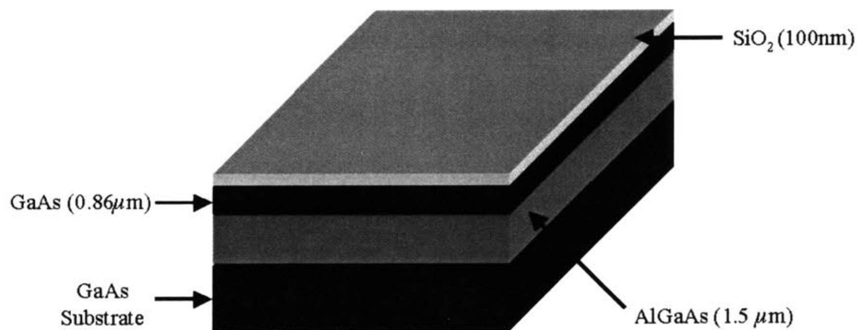

Figure 13. Initial material system of PBG structure

When the growth is finished, the sample is transferred to the Intro chamber which is then vented. A piece of the sample is cleaved and the thickness of the epitaxial growth is verified using x-ray diffraction. Then, a 100 nm thick layer of SiO_2 is evaporated on the sample using an ebeam evaporator. The advantage of using an ebeam evaporator over be inductive or resistive evaporators is that it avoids contamination from the heating up of the crucible and the outgassing of coupling wires.[14] In an E-beam evaporator, a tungsten filament is heated, which makes electrons boil off with high flux. The filament is put far way from the sample to avoid contamination. The high flux electron beam passes through deflection plates and a bending magnet , which bends it 270° and makes it incident onto the surface of the charge. As a result, the charge in the crucible melts and becomes evaporated on the sample. To deposit oxide on the grown sample, an SiO_2 target is put into the crucible of the evaporator, which is then put under vacuum.

The thickness of the evaporated oxide and its refractive index was checked using ellipsometry, in which a circularly polarized beam of light is reflected off the oxide surface at an angle and the resulting change in polarization is measured. Because different thicknesses can produce same intensity change, the measurements are done at different incidence angles and the incident and reflected intensities are compared. Ellipsometry on the evaporated sample piece gave a thickness of 96.7 nm.

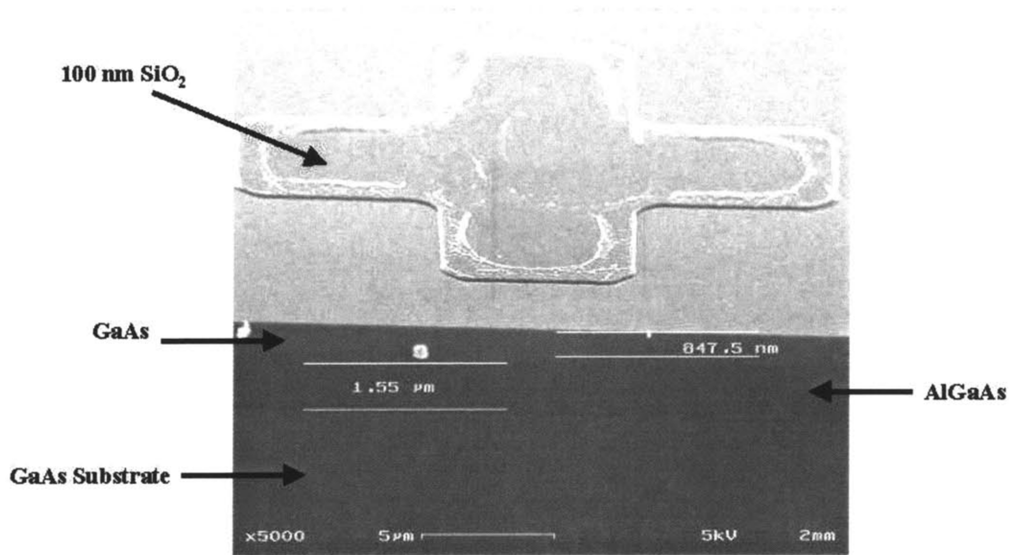

Figure 14. SEM of material system showing the grown structure of AlGaAs, GaAs, and the evaporated SiO_2 which is etched to make a cross shaped alignment mark

II. Direct Write Electron Beam Lithography

Direct Write Electron Beam Lithography is used to define the square lattice of dielectric rods. In electron beam lithography systems, electrons are emitted from the cathode of an electron gun through thermionic emission, field-aided emission, thermal field-aided emission, or photoemission. The electrons are focussed into a narrow beam through the use of lens, deflection plates, and aperture arrangements. The direct write lithography can be done using a vector scan or raster scan system. In a vector scan system, the digital location of each area to be exposed is fed to x and y digital to analog converters causing

the beam is directed to those pixels that must be exposed. In raster scan systems, every pixel is scanned serially and a pattern is exposed by opening and closing a shutter.[14]

Limitations on the smallest feature written by an E-beam lithography system arises from the size of the focussed beam as well as proximity effects. When a pattern is being written, forward and backscattered electrons can expose nearby areas that are not intended for exposure. The beam becomes broadened because of forward scattering, which occurs over a small range of angles with respect to the incident velocity. Backscattering results in a large area fog of exposure.[16] A disadvantage of E-beam lithography systems is their small throughput due to the significantly longer write-time compared to contact or proximity lithography.

In this project, E-beam lithography is used to make these structures because optical lithography will not be able to properly produce features that are smaller than the wavelength of light. E-beam lithography was done by using an IBM VS2A Scanning Electron Beam Lithography (SEBL) system, which has 50 kV external potential applied to accelerate electrons from the source. This vector scan system is capable of having a beam spot size as small as 60 nm. To perform a write, the system breaks the pattern into fields as small as 100 μm, which are exposed individually and stitched together. In order to write patterns within a field, electric and magnetic fields deflect the beam to the pixels that need to be exposed. To move from one field to another, the stage is physically moved under a laser interferometer control.

The waveguide patterns are generated with a Computer Aided Design (CAD) tool using the simulated design parameters. The field size determines the actual pixel size,

which is the incremental step of the electron gun. A field size of 250 μm is used, which gives a pixel size of 15 nm (2^{14} pixels in a field). The patterned area of the file correspond to the area where the direct E-beam write takes place. From simulation, the optimal diameter of each rod is determined to be 300 nm. Nevertheless, E-beam write doesn't exactly simulate the pattern as designed with CAD due to proximity effects (forward and back-scattering of electrons) as well as the error introduced during the movement of the beam and the stage. To account for these effects, the patterns are programmed to be about 60 nm smaller than the desired size. Thus, in order to account for discrepancies as well as to cover a test frequency range, patterns with diameter ranging from 270 nm to 330 nm are designed.

Before the E-beam lithography exposure, each sample is coated with a 200 nm thick layer of polymethylmethacrylate (PMMA). The coating is done by spinning a droplet of PMMA (solution of 3% by value in chlorobenzene) on the sample at 3600 rpm for one minute and baking it for one hour at 180°C. Next, a thin 5 nm layer of chrome is evaporated on the sample. This conductive layer eliminates sample charging, which can deflect the beam, thus resulting in pattern elongation. The design parameters are made as accurate as possible through dose experiments, which include varying beam current, field size, and intensity values. A dose of 537 $\mu C/cm^2$, current of 50 pA, and clock frequency of 0.04 MHz produced holes with the desired diameter.

Then, the chrome is etched off the written sample by submerging it in a Cr-7 photomask remover solution for 15 seconds. The exposed PMMA is developed using 90 second rinse in methyl-isobutyl-ketone (MIBK), which dissolves the exposed part of the

PMMA layer and leave behind patterned holes; this is followed by a 30 second rinse in isopropanol (IPA). Finally, the sample is inspected using a Scanning Electron Microscope (SEM) to determine the size of the holes (Figure 15).

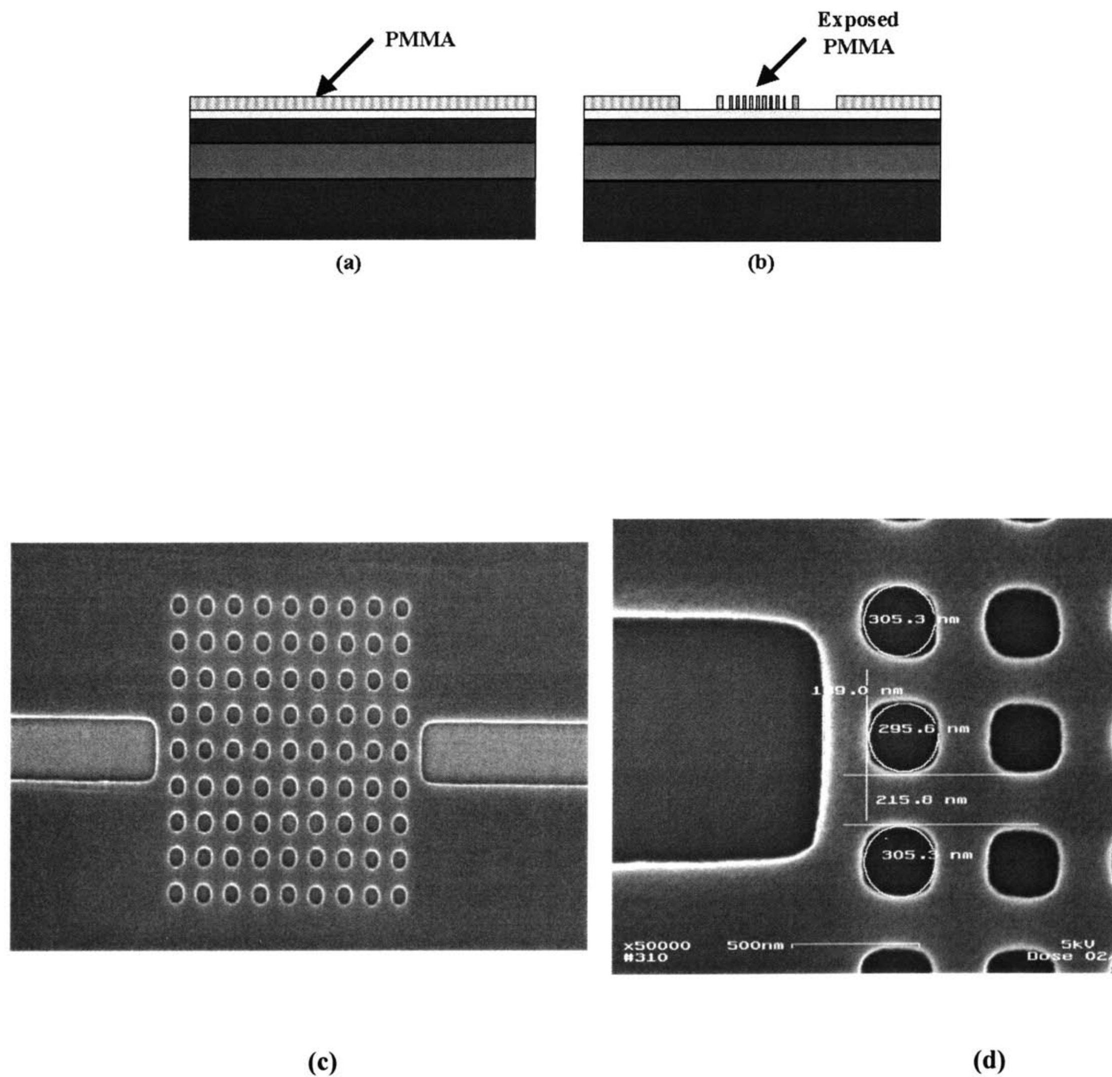

Figure 15. a) PMMA before exposure b) PMMA after exposure

c,d) SEM of patterned PMMA with average hole size of 300 nm and input waveguide width of 1 μm

III. Photolithography

After the PMMA is developed, a 30 nm thick nickel layer is evaporated on the samples. This process is necessary to provide a metal mask for the oxide etch that follow. The nickel evaporation leaves the sample coated with nickel, and a liftoff process strips off the PMMA with the nickel that is on top it (Figure 16 a). To perform the liftoff, 1-methyl-2-Pyrrolidinone (NMP) solution is heated up to 80°C in a beaker. The sample is then put into the beaker and touched carefully with smooth swaps to enhance the nickel removal. To ensure a successful liftoff process, the beaker was placed in an ultrasonic bath for 30 minutes. Finally, the sample is rinsed with acetone and methanol, and dried with a nitrogen gun. This process leaves behind a 2D array of 30 nm thick nickel cylinders, and nickel waveguides that are 120 μm long, 1 μm wide, and 30 nm thick (Figure 16b).

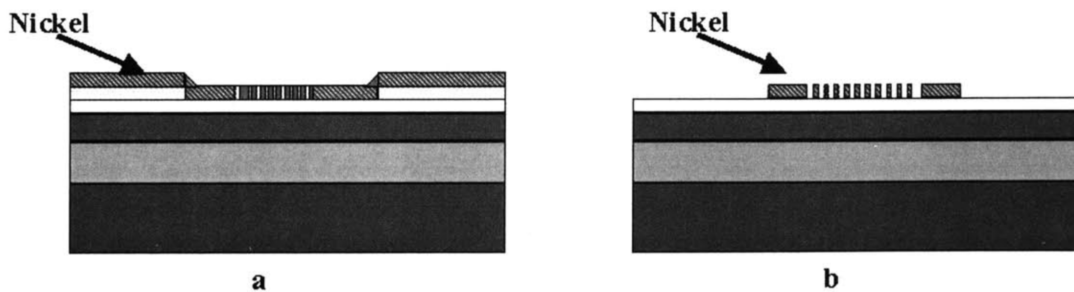

Figure 16. Sample a) after nickel evaporation b) after nickel liftoff

The input and output waveguides are required to be much longer than 120 μm for cleaving and testing purposes. However, writing a large number of long waveguides by

E-beam takes a very long time. Photolithography, which is a faster process with higher throughput, can be used to extend the waveguides longer. Photolithography consists of two steps. First, the patterns are created with the desired features using chrome on a quartz plate. The second step is a chemical process, in which a sample is coated with photoresist, exposed with ultraviolet (UV) light, and then developed with an alkaline solution (for positive resist).

Photoresist is a mixture of a photoactive compound (PAC), a matrix material, and a solvent. The matrix material, which is a thick resin of a long chain polymer, acts as the base material. The solvent helps control the mechanical properties such as viscosity. The PAC, which usually is diazoquinone (DQ) in positive resist, acts as an inhibitor before exposure. The PAC and the matrix material are chemically bonded at the surface of the resist. During exposure, the weakly bonded N_2 in the PAC is liberated. Then, a Wolff rearrangement takes place to stabilize the structure and forms ketene. When the solution reacts with water, it is converted into carboxylic acid. During the reaction with a base solution, the carboxylic acid breaks into water soluble amines.[14] Thus, the exposed region is removed.

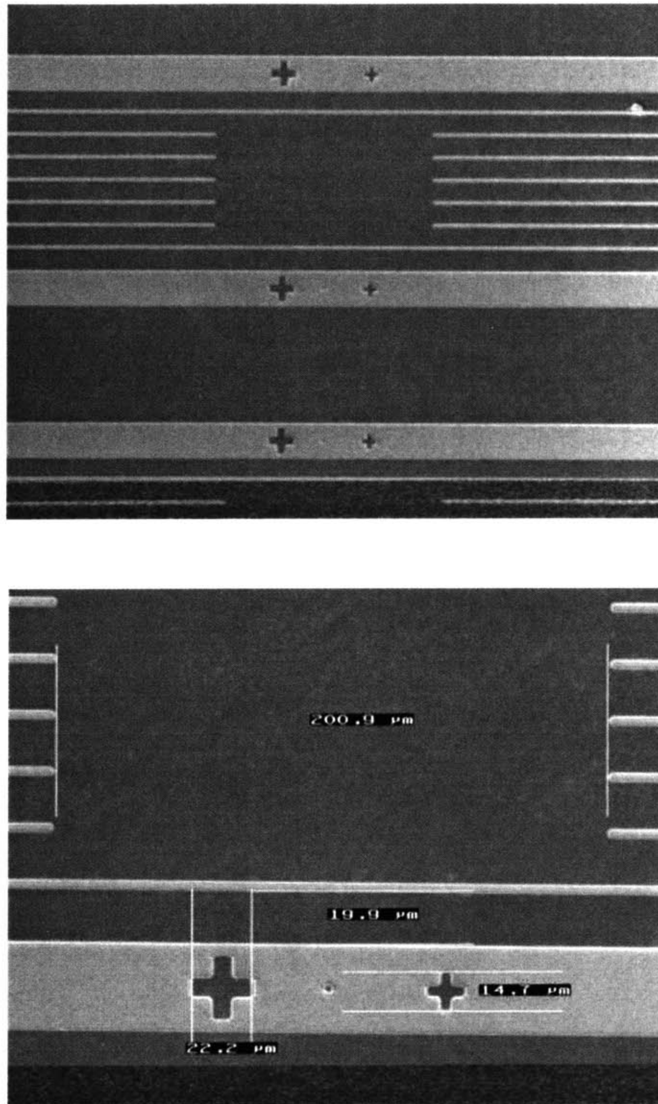

Figure 17. SEM of a sample after UV exposure. Figure shows some of the mask patterns that have been transferred to the photoresist.

Waveguide patterns with width ranging from 1 μm to 3 μm are designed on a 5-inch mask (Figure 17). Some of the device have one input and two outputs. Some of the waveguides are straight and some are curved to couple out light from the sharp bends. Due to the various designs and the small feature patterns, it was easier to make a dark field mask written by E-beam.

The samples with the nickel patterns are put in a hexamethyldisilazane (HMDS) oven. This process helps to promote adhesion of photoresist to the sample. Next, a drop of Shipley 1813 positive photoresist is spun on the sample at 4000 rpm for 30 seconds, which results in a layer that is approximately 1.3 μm thick (Figure 18 a). Then, the sample is prebaked for 30 minutes to harden the resist.

The box shaped nickel alignment marks, which were written by E-beam with the PBG crystal, are visible through the resist layer. The alignment marks on the mask are crosses, whose size and position were designed in such a way that the box marks on the sample would fit around them. The cross-box patterns vary from 6 μm to 24 μm in size, which improves the focussing during the alignment process. By aligning the crosses with the boxes on the samples, the nickel coated waveguides are aligned with the waveguide patterns on the mask. This alignment process is difficult due to the resolution limit of the aligner. However, it is a crucial step because coupling loss, which would result from inaccurate alignment, has to be minimized.

Next, the resist is exposed to UV light through the clear part of the mask. Using vacuum contact, a 50 second exposure at 6 mW of power yields a patterns that are not over or under exposed. The samples are then developed in a Shipley MF-319 solution, which removes the exposed regions of the photoresist (Figure 18 b). One minute of development and a one minute rinse in deionized water results in a sample that is not over or under-developed.

After the samples are examined using an optical microscope, another nickel evaporation and liftoff is performed to coat the newly defined input and output waveguides. The liftoff process leaves behind long waveguides and a 2D PBG crystal coated with nickel (Figure 19).

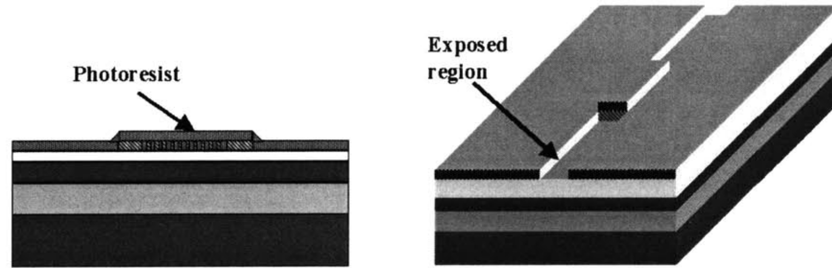

Figure 18. Sample a) after spinning photoresist b) after exposure and development

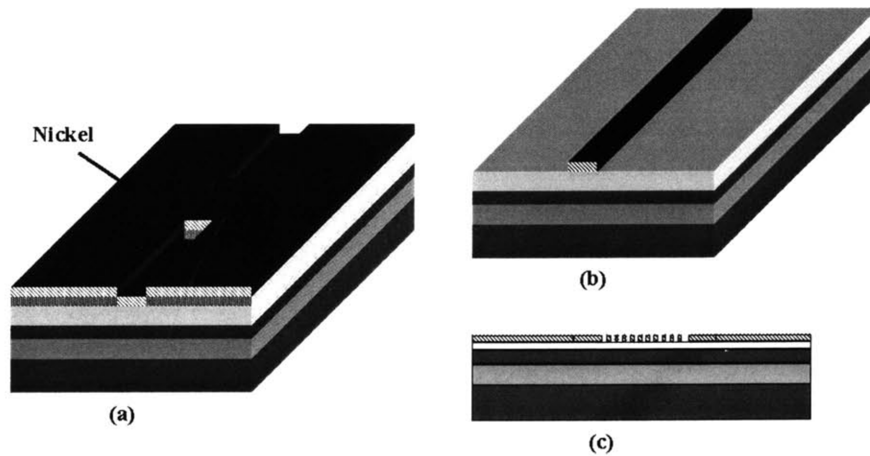

Figure 19. Sample after a) nickel evaporation b, c) nickel liftoff

IV. Etching

Material systems can be patterned and etched by using wet or dry etch mechanisms. Wet etch is a purely chemical process that usually consists of three process. First, the etchant species move to the surface of the sample. Second, a chemical reaction with the part of the sample that is not covered with a mask produces soluble byproducts. Third, these products move away from the surface of the sample. In order to facilitate etching, the solution is usually heated and stirred. Wet etch results in isotropic sidewalls.

Dry etches, which produce anisotropy and high selectivity, can be done in a reactive ion etcher (RIE) or a high density plasma etcher. RIEs are capable of generating ion density of 10^9 cm^{-3}. In conventional parallel plate RIE systems, radio frequency power is put into a thin sheath region around the electrode by capacitive coupling. A plasma starts as the radio frequency power accelerates electrons in the vertical direction. The electrons collide with gas molecules and cause electron-impact dissociation and excitation which sustains the plasma. As a result, the sustained plasma will have many positive ions, few negative ions, radicals, and some neutral atoms. Because the electrons have lighter mass, they are able to move a larger distance compared to the ions. During the process, the electrons collide with the electrode and the sidewall, thus inducing a self-bias. This bias causes an electric field which forces many of the ions to accelerate and bombard the sample. In RIEs, the ion density is coupled with the ion energy; to achieve a higher density of ions, higher RF power is required to ionize more molecules. However, the higher power causes a larger electric field and ion bombardment can damage the sample.

Advanced plasma etching techniques generate higher ion density by separating the power from the ion density. Electron cyclotron resonance (ECR) etchers use an external magnetic field and a resonance effect to confine the electrons. Resonance occurs in the systems when the applied microwave frequency is equivalent to the orbital frequency of electrons under an external magnetic field. The resonance accelerates the electrons and increases their mean free path before they collide with the electrode. As the electrons travel a longer distance, they are able to dissociate and excite more molecules, which produces a higher plasma density (10^{12} cm^{-3}). The ion energy is controlled separately by power applied to the electrode. Another advanced technique is inductively coupled plasma (ICP) etching, in which a RF current circulating around the chamber in opposite directions causes an alternating magnetic field in the vertical direction. This induces a RF electric field, which accelerates electrons in a circular path and confines them in a circular motion. The circular motion of the electrons give them a longer mean free path and minimizes their collision with the electrode and the sidewall. The energy of the ions is controlled by applying another RF source to the electrode, which helps to reduce ion bombardment of the sample.

In the PBG fabrication process, the 100 nm thick SiO_2 layer which has patterned nickel mask is etched first. Then, the nickel mask is removed using a wet etching process and the patterned oxide is used as a mask to etch the GaAs/AlGaAs layers.

A Fluorine containing gas is required to etch Si and SiO_2. The etch of the SiO_2 mask is done in the NanoStructures Lab (NSL) using a PlasmaTherm RIE, which has helium (He), oxygen (O_2), trifluoromethane (CHF_3), and tetrafluoride (CF_4) gas lines.

Before the etch, the chamber is cleaned using 4 sccm of CF_4 and 20 sccm of O_2, striking the plasma at 25 mT pressure with 350 V DC bias. The etching is performed at 10 mT pressure, 300 V DC bias using 15 sccm of CHF_3 (Figure 20 and 21). The etch rate was measured to be 17 nm per minute.

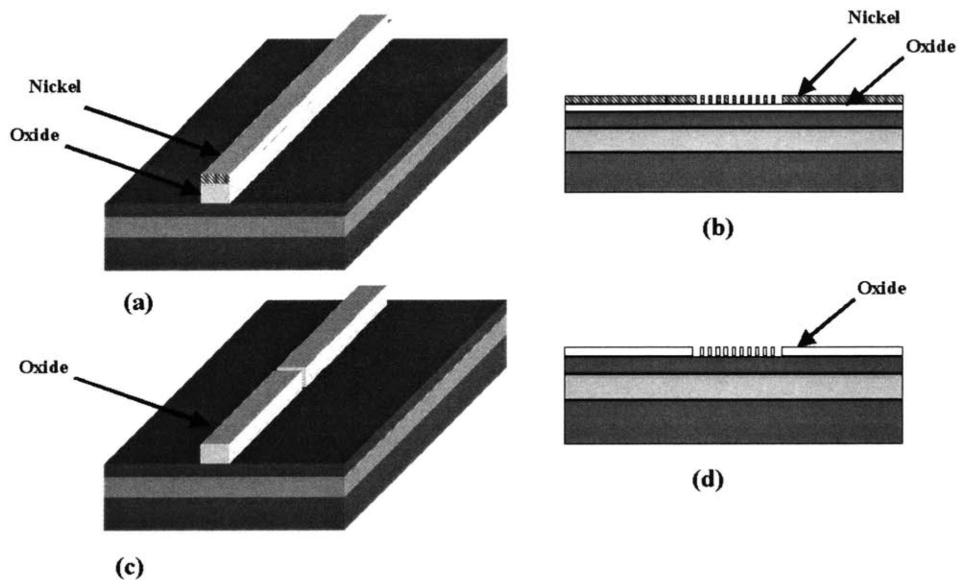

Figure 20. a) sample after oxide etch b) cross section of (a)

c) sample after nickel wet etch d) cross section of (c)

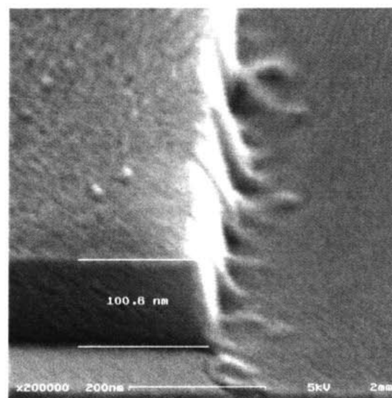

Figure 21. SEM of oxide mask after nickel wet etch (the nickel has not been completely lifted off the side-wall)

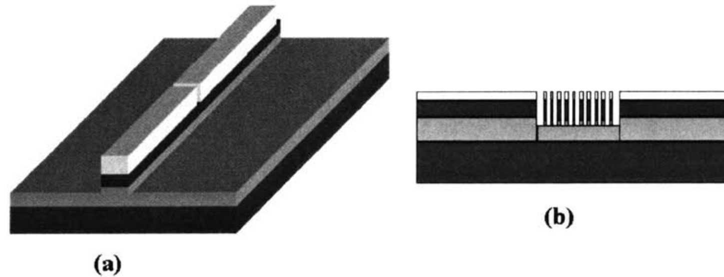

Figure 22. a) sample after GaAs/AlGaAs etch b) crossection of (a)

After the etch of the oxide mask, the nickel mask is removed using a wet etchant (Figure 20 and 21) which contains nitric acid. The next step in the process is to etch the GaAs and AlGaAs layers using the oxide mask (Figure 22) to a depth of 1.5 μm. The first etch experiment was done in the NanoStructures Lab (NSL) using a parallel plate RIE which has a chlorine (Cl_2) line. The first etch was done at 50 W (resultant DC bias of 100 V), 20 mT pressure, and 40 sccm of Cl_2 for 10 minutes. Deposition on the edges of the mask was observed and the trench surface was not very smooth (Figure 23 a). In addition, the etch was not isotropic and underetching had taken place.

In the next trial, the pressure was reduced to 5 mT. This resulted in the destruction of the oxide mask (Figure 23 b). Electrons had a higher mean free path due to the presence of fewer molecules in the chamber (thus less collision); they were able to directly couple to the electrode and cause a higher DC bias. As a result, the ionized molecules are accelerated with high energy and bombarded the sample.

The addition of He to reduce the chlorine partial pressure did not help the process (Figure 23 c). Even though it helped the mask to hold up, the etch of GaAs was uneven. This was because at a very low pressure, the etch limiting step is the adsorption and chemical reaction, which is the slowest step due to the small concentration of reactants. The ionized Cl atoms are transported away from the sample before there was enough time for them to arrive at and to react with the surface of the GaAs sample; since the Cl atoms are larger, they are easily pumped out when the system tries to maintain the low pressure. Instead, the smaller He atoms are accelerated to the sample. The mask was not damaged because the lighter (yet many) He atoms and the larger (yet fewer) Cl ions did not cause much physical etch.

In the next trial, the He was removed and the average pressure was increased to 13 mT (Figure 23 d). Even though the mask held up, polymer was deposited at the edge of the mask. Furthermore, the inside of the trench was very rough and full of "grass". Reducing the flow to 25 sccm and the pressure to 5 mT did not impact the etch (Figure 23e). In the trenches, chemical etching was insufficient while the high DC bias (115V) caused a stronger physical etch.

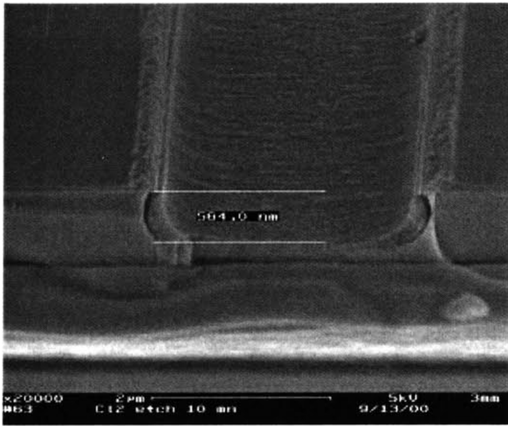

a

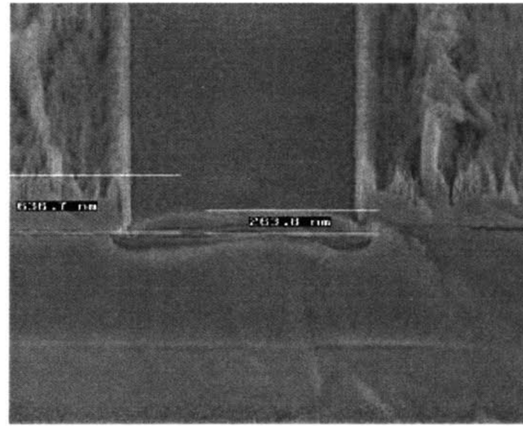

b

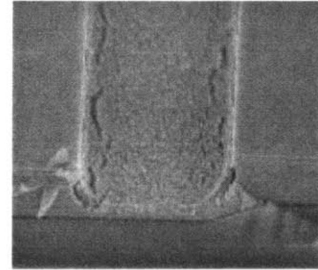

c

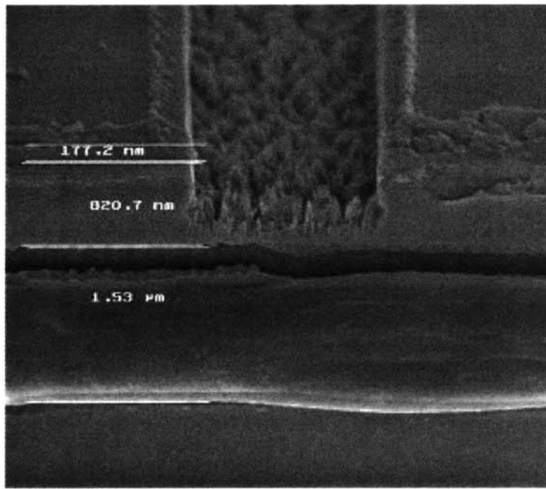

d

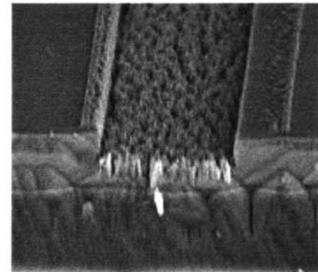

e

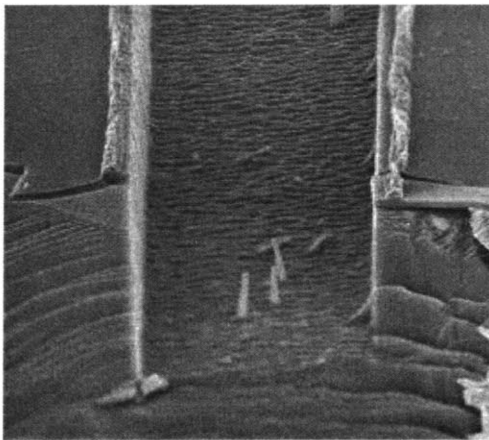

f

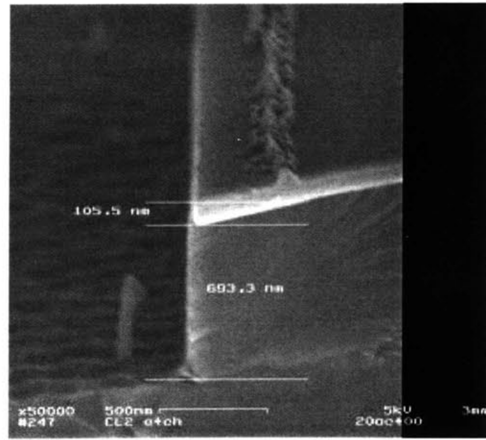

g

Figure 23. GaAs/AlGaAs etch data in NSL

TABLE 1. NSL Etch Results

	Pressure (mT)	Power (W)	DC Bias (V)	Flow (sccm)	Time (min)
Figure 23(a)	20	50	100	40 sccm of Cl_2	10
Figure 23(b)	5	50	115	40 sccm of Cl_2	10
Figure 23(c)	5	50	115	40 sccm of Cl_2 10 sccm of He	10
Figure 23(d)	13	50	115	40 sccm of Cl_2	10
Figure 23(e)	5	50	115	40 sccm of Cl_2	10
Figure 23(f)	5	26	70	20 sccm of Cl_2	16
Figure 23(g)	5	26	70	20 sccm of Cl_2	16

Finally, the power was lowered to 26 W and the flow was lowered to 20 sccm to operate at 5 mT. This recipe yielded a good etch with a resultant etch rate of 43 nm/min. The DC bias was as low as 70 V, which reduces the unwanted bombardment of the sample. Also, the smaller flow allowed a smooth chemical reaction at the surface while maintaining low pressure. The inside of the trench was a bit rough and some deposition was observed on the edges of the mask (Figure 23 f, g). The sidewalls were very straight. This etch can be improved by slightly adjusting the etch parameters by a small amount. The polymer also may be removed by ashing the sample in an O_2 plasma.

The next etching experiment was done in the Exploratory Materials Laboratory (EML) using the PlasmaTherm RIE\PECVD (Series 700). The system has gas lines for borontrichloride (BCl_3), chlorine (Cl_2), silicon tetrachloride ($SiCl_4$), helium (He), oxygen (O_2), trifluoromethane (CHF_3), tetrafluoride (CF_4), methane (CH_4), and nitrogen (N_2). In the first trial, 30 sccm of BCl_3 was used at 15 mT pressure and 250 W power (resulting in 350 V DC bias) for 11 minutes (Figure 24 a,b). The etch suffered from micromasking.

After some etch happened near the oxide mask, the oxide sputtered off and covered part of the etched GaAs; this new layer of oxide acted as a mask and caused stepped etching. In the 20 μm trenches, the etched surface becomes smoother as one moves away form the oxide mask. However, micromasking is a severe problem in the 1 μm trenches; the oxide almost acts as a mask everywhere in the narrow trench and etching barely takes place.

When the flow was reduced to 15 sccm BCl_3 and the pressure was increased to 20 mT, "grass" was formed in the big trenches while the GaAs in the small trenches was not etched (Figure 24 c). At higher pressure, the limiting step becomes desorption, which is a slower process; there is a a high number of reactants and a lower sputtering voltage. Increasing the pressure allowed a higher number of reactants in the chamber and slowed down the removal of resultant polymer material, which prevented the etching.

The flow was increased to 20 sccm BCl_3 and the pressure was reduced to 8 mT. Even though the low pressure drove off most of the deposition at the edge, etching didn't take place inside the trenches (Figure 24 d). The inside surface and the sidewall of the trenches were very rough. This was because the flow was too high for the required low pressure; most of the BCl_3 ions did not have enough time at the surface for reaction prior to being transported away.

Thus, the flow was reduced to 5 sccm and the pressure was set to 8 mT. This resulted in a very nice etch (Figure 24 e,f) and the mask held up well. The sidewalls were straight and passivated by some polymer. Moreover, the inside of the trenches was very smooth, and almost all of the polymer was removed.

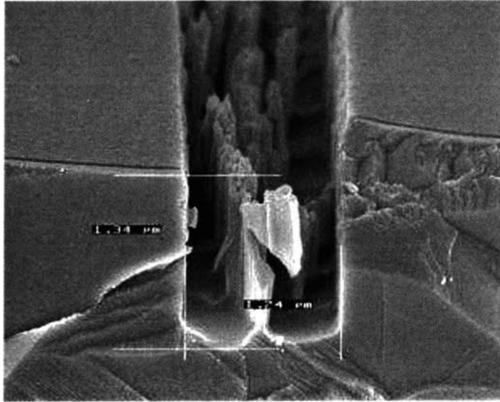

a

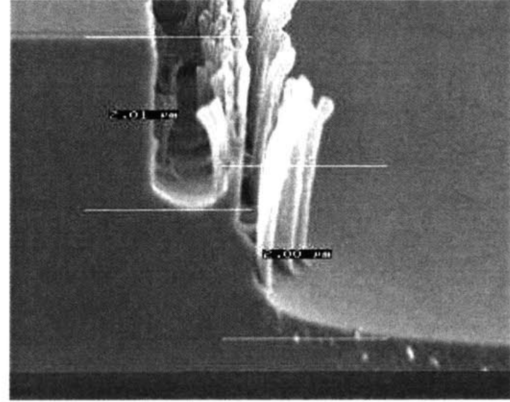

b

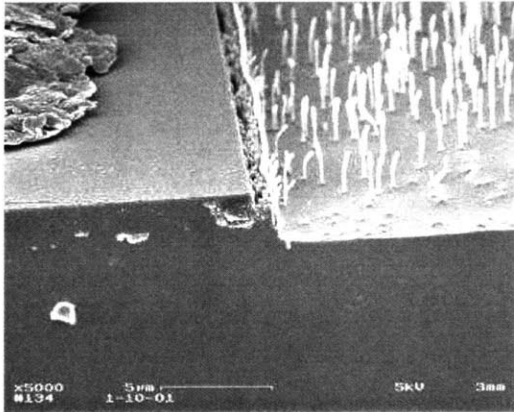

c

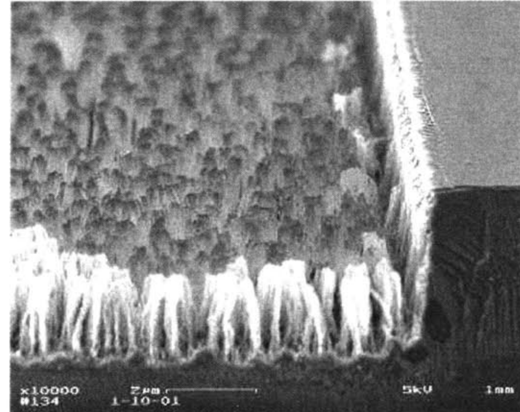

d

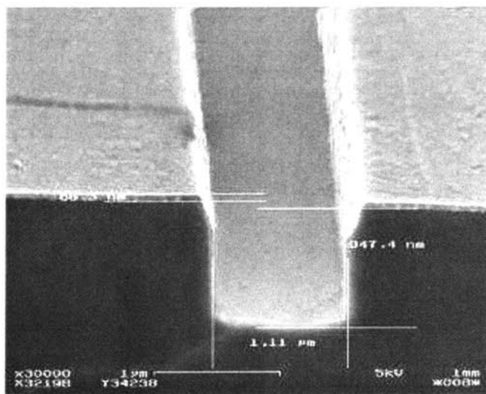

e

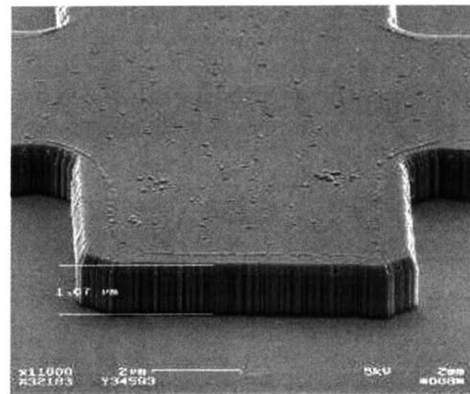

f

Figure 24. GaAs/AlGaAs etch in EML

Table II. EML Etch Results

	Pressure (mT)	Power (W)	DC Bias (V)	Flow (sccm)	Time (min)
Figure 24(a)	15	250	350	30 sccm of BCl_3	11
Figure 24(b)	15	250	350	30 sccm of BCl_3	11
Figure 24(c)	20	250	175	15 sccm of BCl_3	11
Figure 24(d)	8	250	370	20 sccm of BCl_3	10
Figure 24(e)	8	250	400	5 sccm of BCl_3	11
Figure 24(f)	8	250	400	5 sccm of BCl_3	11

V. Oxidation

The final fabrication step in the process is the oxidation of the AlGaAs layer into Al_xO_y (Figure 25). The sample is place in a quartz boat and inserted into a quartz tube which is heated by a furnace. The temperature of the furnace is set to the desired value. A flow of nitrogen is used to carry water vapor from a bubbling water bath to the sample. In order to achieve the required oxidation rate, the nitrogen flow, furnace temperature, position of sample and sample boat, and the temperature of the water are carefully controlled. The resultant index contrast between Al_xO_y and the GaAs layer provides modal confinement in the vertical direction.

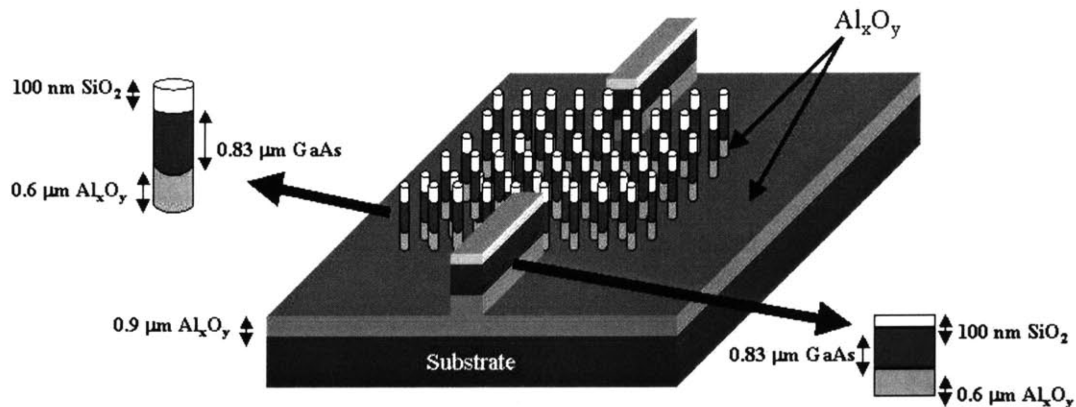

Figure 25. Final profile of PBG structure

Chapter IV

Conclusion and Future work

1. Fabrication conclusion

a. Electron Beam Lithography and Photolithography

The photolithography process includes a step where the mask needs to be aligned with features that are written by E-beam lithography. Alignment marks on the mask and on the sample are aligned prior to the exposure so that the E-beam written waveguides becomes directly aligned with those done by photolithography.

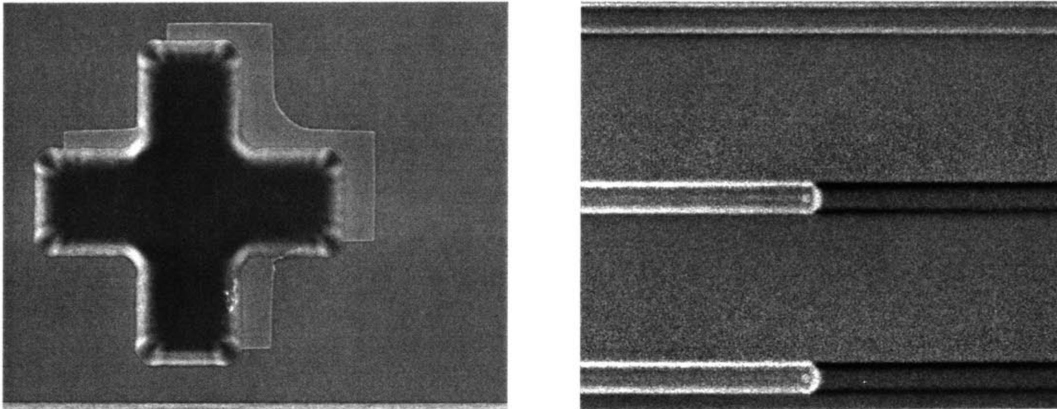

Figure 26. Misaligned cross shaped alignment marks (left); the background cross is written by E-beam and covered with nickel while the cross on the foreground is unexposed photoresist. Alignment of 1 μm lines (right). The left section is exposed photoresist lines while the right section is E-beam written and nickel coated lines.

However, problems are encountered during the alignment process (Figure 26). First, using a dark field mask made it difficult to find the nickel coated small features that were written by E-beam lithography. After the patterns are located using the clear windows on the mask, correcting the offset due to rotation was very difficult. The aligner is capable of one μm resolution; thus, trying to align one μm pushed the aligner to its limit yielding poor results.

In order to solve this problem, all the input and output coupling waveguides are currently being written by E-beam lithography. However, E-beam lithography has a lower throughput, which means that it takes longer to write the waveguides. In order to avoid a long write time, the beam current used for the long waveguides is changed to 940 pA while the PBG region is still written with 50 pA. The clock frequency used for the new current is 0.75 MHz while that for the PBG region remains the same as before (0.04 MHz). The faster clock speed implies that shorter time is taken to write the long input and output waveguides. In order to accommodate for the larger beam size which increases proximity effect, the waveguides are designed with smaller width in CAD.

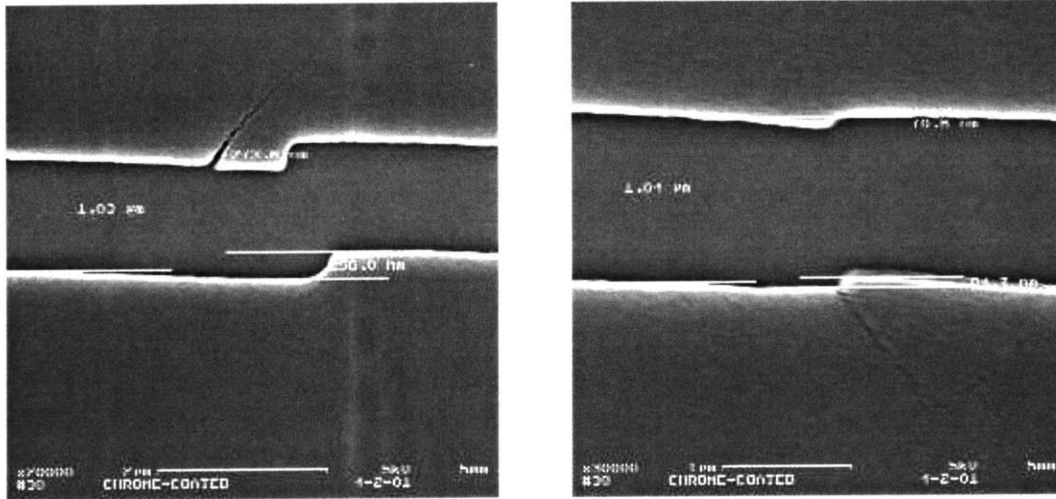

Figure 27. Stitching error between two field written with two different beam currents (left) and stitching error between two fields written with the same beam current (right)

This method has resulted in two distinct stitching problems. The first problem is stitching error between the fields written with the different beam currents. There seems to be a huge misalignment between the fields written by 50 pA and 940 pA beam current (Figure 27 left). The second problem is stitching error between the fields that are each written at 940 pA. Since the waveguides are long, there are 17 fields written and stitched together using 940 pA; however, a larger alignment error is observed at the boundary between the fields (Figure 27 right).

The stitching problem between the fields written at 50 pA and at 940 pA could be due to machine calibration error during the beam current change. The stitching error between the fields that are written at 940 pA, could be a result of the big field size. Furthermore, the magnetic field of E-beam system might not be strong enough to deflect the electrons all the way to the border of the large 250 μm field. In order to solve these prob-

lems, new experiments are currently being carried out. Test patterns that are 1 μm wide are written and stitched together using a beam current of 940 pA and with both 50 pA and 940 pA. These patterns are written on field sizes of 100 μm, 150 μm, and 250 μm.

b. Deep Etch

Currently, the deepest etch that has been done is approximately 1.1 μm while the required etch depth is 1.5 μm. After the 1 μm limit, the AlGaAs does not etch regularly. Small one micron wide trenches are etched smoothly and with straight sidewalls. However, the 20 μm wide trenches had a very rough surface (Figure 28 a). From the results, it can be observed that there is a trend for a deeper etch AlGaAs at the region where there is a higher content of unetched GaAs.

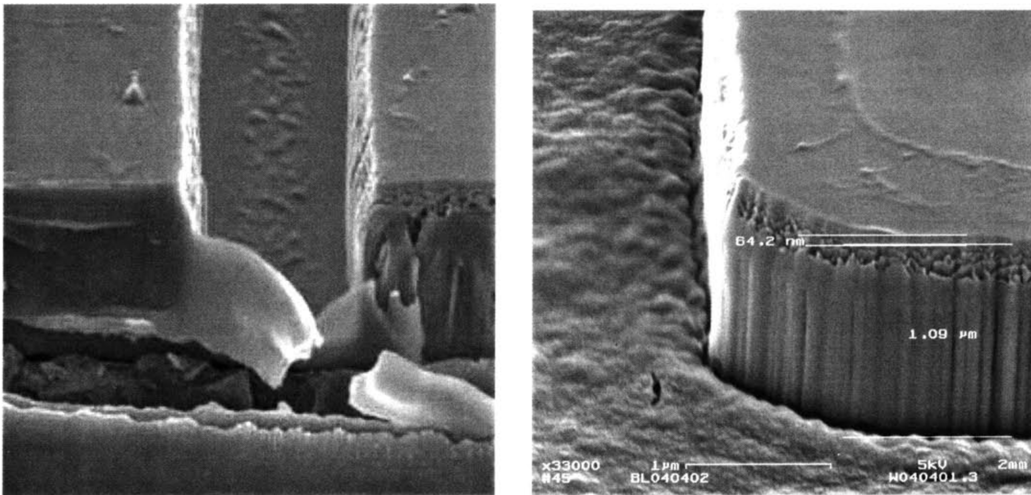

Figure 28 a) 15 minutes straight etch of GaAs/AlGaAs layers (no interval)

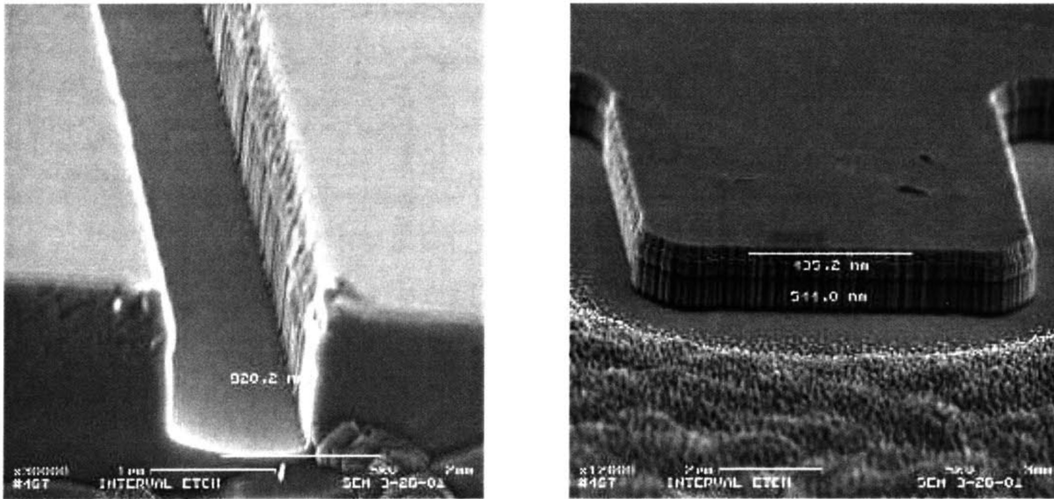

Figure 28 b) Interval Etch of GaAs/AlGaAs layers

In order to investigate if the problem was a result of sample heating, an interval etch was done. A 5 minute etch was followed by a 2 minute flow of gas and another 5 minute etch. However, the same roughness was observed even though it was reduced to a smaller scale (Figure 29 b). The problem could still be a result of heating. The heat exchanger that cools down the etcher has been experiencing problems and is being fixed. A new experiment will be carried out in which a longer cooling cycle will be used.

c. Process Flow

The rest of the steps in the process flow have been developed successfully. Recipes with the correct parameters have been compiled. Currently, samples are being run through the all of the steps as a proof of concept. The samples are carefully examined using an optical microscope and SEM after each step.

2. Future work

a. Lapping and Cleaving

In order to test the structures, the samples need to have smooth facets so that light will not randomly scatter away at the input and output facets. These clean and smooth facets can be achieved by lapping the sample before cleaving. Lapping will thin the sample by reducing it from the original size of approximately 400 μm to a thickness that is less than 200 μm. The thinner substrate will reduce unwanted cleave propagation.

The lapping step will be done before the oxidation step. This is because previous work has revealed that the Al_xO_y layer gets stripped of during the lapping process. Lapping will be done by mounting the sample on a glass slide with a wax and polishing the backside with a solution composed of polishing grit, household detergent and water. Cleaving can be done by making marks using a diamond scribe and propagating the cleave by applying pressure. However, purchasing a better cleaving system is being considered currently.

b. Testing PBG Devices

The fabricated PBG devices will be tested in order to explore their actual band gap and compare it with simulated values. Since the fabrication does not produce the exact size of the simulated PBG rods, the observed band gap could be slightly shifted away from the simulated values. The existence of a band gap is verified by testing structures with varying number of columns as mentioned in Chapter II; this test will show the widening of

the PBG as the number of columns increases. The available test equipment at MIT has a test range of 1390 nm to 1680 nm (0.2976 (c/a) to 0.3597 (c/a) for a lattice constant, a, of 500 nm), which safely covers the simulated frequencies in the first and second bands, thus showing both edges of the band gap, which ranges from 0.2998 (c/a) to 0.3224 (c/a).

Next, PBG slab waveguides with linear defects will be tested (Figure 29). This test will show the localization of the defect mode in the band gap. The defect rods are made by changing the diameter of a column of rods in the CAD design before the E-beam lithography exposure. The defect mode is expected to have a center frequency of 0.317 (c/a). To evaluate efficiency, the output of the linear defect will be compared with the output of a straight slab waveguide.

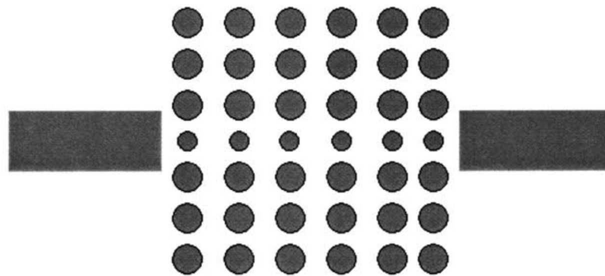

Figure 29. Linear PBG waveguide

Then, the 90° sharp bend PBG waveguides will be tested. To make detection of output light possible, the output coupling waveguides are designed in two ways. The first design has two straight waveguides coupling into and out of the photonic crystal. In the photonic crystal, two 90° bends are joined together, making the light to go through a total

of 180° bend (Figure 30 a). In the second design, the light couples into the photonic crystal from a straight waveguide. Then, it goes through a 90° bend in the photonic crystal and couples out by going through a curved slab waveguide (Figure 30 b). The output fom the sharp bend PBG waveguides is normalized by using the output from the linear PBG waveguide.

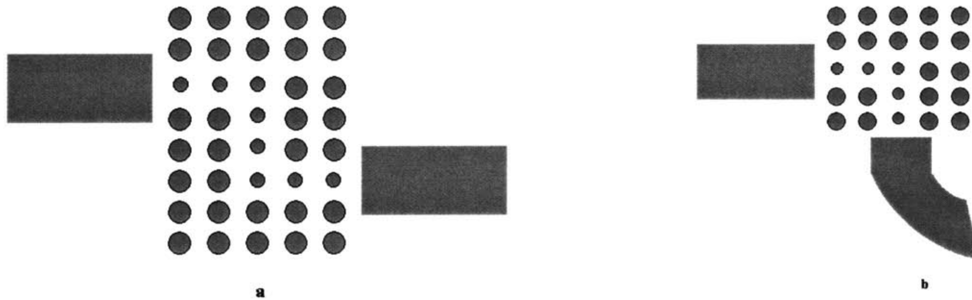

Figure 30. a) a total 180° PBG bend with straight input and output couplers b) a 90° PBG bend with a curved output coupler

Coupling into and out of the photonic crystal is still a problem being investigated. Light can be lost to radiation modes at the junction between the photonic crystal and the coupling waveguides due to reflection and scattering from the photonic crystal waveguide ends. A tapered guide, whose width is adiabatically reduced, can be designed in such a way that its end goes into the photonic crystal. A conventional straight waveguide can be used as an output coupler. Another alternative is using an inverse tapered out-coupler that protrudes out from the photonic crystal (Figure 31). Simulation of these methods of coupling show a high transmission.[17]

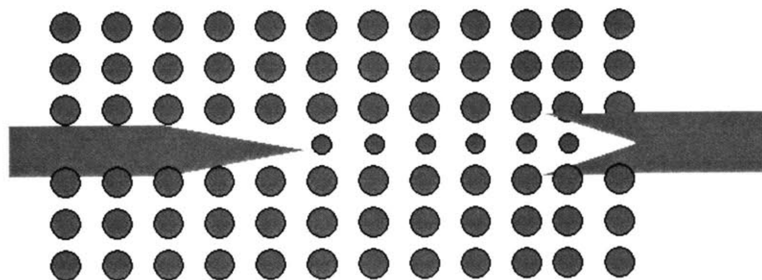

Figure 31. Tapered input and output coupling waveguides

References

1. Y. Fink, A. Urbas, M.G. Bawendi, J.D. Joannopoulos, E.L. Thomas, "Block Copolymers as Photonic Band Gap Materials," J. Lightwave Tech., 17, 1963-1969, (JLT IEEE special issue on photonic crystals-invited paper).

2. S. G. Johnson, S. Fan, P.R. Villeneuve, J.D. Joannopoulos, and L.A. Kolodziejski, "Guided modes in photonic crystal slabs," Phy. Rev. B **60** 5751 (1999).

3. J. D. Joannopoulos, R. D. Meade, and J. N. WInn, *Photonic Crystals* (Princeton, New York, 1995).

4. J. A. Kong, *Electromagnetic Waves Theory* (Cambridge, Massachusetts, 1998).

5. D. M. Whittaker, "Scattering-matrix treatment of patterned multilayer photonic structures", Phy. Rev. B **60** 2610 (1999).

6. R. D. Meade, A. M. Rappe, K. D. Brommer, J. D. Joannopoulos, and O. L. Alerhand, Phys. Rev. B **48**, 8434 (1993).

7. Piere R. Villeneuve, Shanhui Fan, and J. D. Joannopoulos, "Microcavities in photonic crystals: Mode symmetry, tunability, and coupling efficiency", Phy. Rev. B **54** 7837 (1996).

8. Shanhui Fan, Joshua N. Winn, Adrian Devenyi, J. C. Chen, Robert D. meade, and J. D. Joannopoulos, "Guided and defect modes in periodic dielectric waveguides", Opt. Society of America **12** 1267 (1995).

9. Alongkarn Chutinan and Susumu Noda, "Waveguides and waveguide bends in two-dimensional photonic crystal slabs", Phy. Rev. B 62 4488 (2000).

10. J. N. Winn, "Dynamic studies of photonic crystals," M.S. thesis (Massachusetts Institute of Technology, Cambridge Mass. 1994).

11. T. P. Orlando, S. D. Senturia, and P. L. Hagelstein, *Physics of Solid State Application* (M.I.T., 2000).

12. S. G. Johnson, S. Fan, P. R. Villeneuve, J. D. Joannopoulos, and L. A. Kolodziejski, "Guided modes in photonic crystal slabs", Phy. Rev. B **60** 5751 (1999).

13. A. Mekis, J. C. Chen, I. Kurkland, S. Fan, P. R. Villeneuve, and J. D. Joannopoulos, "High Transmission through Sharp Bends in Photonic Crystal Waveguides", Phys. Rev. Lett. 77, 3790 (1996).

14. Stephen A. Campbell, *The Science and Engineering of Microelectronic Fabrication* (Oxford University Press, New York, 1996).

15. Conversation with Dr. Gale Petrich, CBE Group Research Scientist.

16. Submicron and Nanometer Structures Technology (6.781) class notes at MIT.

17. J.D. Joannopulos, S. Fan, A. Mekis, and S.G. Johnson, "Novelties of Light with Photonic Crystals".

18. Alexei A. Erchak, "Design and Fabrication of Light Emitting Diode Using a Two-Dimensional Photonic Crystal," M.S. thesis (Massachusetts Institute of Technology, Cambridge Mass. 1999).

19. Kuo-Yi Lim, "Design and Fabrication of Light Emitting Diode Using a One-Dimensional and Two-Dimensional Photonic Bandgap Devices," Ph.D. thesis (Massachusetts Institute of Technology, Cambridge Mass. 1999).

20. R. J. Contolini, "The Temperature Dependence of the Etch Rates of GaAs, AlGaAs, InP, and Masking Materials in a Boron Trichloride:Chlorine Plasma", J. Electrochem. Soc. **235** 929 (1988).

21. S.J. Pearton, "Reactive Ion Etching of III-V Semiconductors", International Journal of Modern Physcis B. **8** 1781 (1993).